ADVANCED MATERIALS
www.advmat.de

Quantum Conductance in Memristive Devices: Fundamentals, Developments, and Applications

Gianluca Milano, Masakazu Aono, Luca Boarino, Umberto Celano, Tsuyoshi Hasegawa, Michael Kozicki, Sayani Majumdar, Mariela Menghini, Enrique Miranda, Carlo Ricciardi, Stefan Tappertzhofen, Kazuya Terabe, and Ilia Valov**

Quantum effects in novel functional materials and new device concepts represent a potential breakthrough for the development of new information processing technologies based on quantum phenomena. Among the emerging technologies, memristive elements that exhibit resistive switching, which relies on the electrochemical formation/rupture of conductive nanofilaments, exhibit quantum conductance effects at room temperature. Despite the underlying resistive switching mechanism having been exploited for the realization of next-generation memories and neuromorphic computing architectures, the potentialities of quantum effects in memristive devices are still rather unexplored. Here, a comprehensive review on memristive quantum devices, where quantum conductance effects can be observed by coupling ionics with electronics, is presented. Fundamental electrochemical and physicochemical phenomena underlying device functionalities are introduced, together with fundamentals of electronic ballistic conduction transport in nanofilaments. Quantum conductance effects including quantum mode splitting, stability, and random telegraph noise are analyzed, reporting experimental techniques and challenges of nanoscale metrology for the characterization of memristive phenomena. Finally, potential applications and future perspectives are envisioned, discussing how memristive devices with controllable atomic-sized conductive filaments can represent not only suitable platforms for the investigation of quantum phenomena but also promising building blocks for the realization of integrated quantum systems working in air at room temperature.

1. Introduction

The exponential growth of electronics and computing capabilities has reshaped our society, where the development of information and communication technologies has opened new prospects for the realization of the Internet of Things (IoT), big data analysis, machine learning algorithms, and artificial intelligence. In the last several decades, continuous device scaling of metal–oxide–semiconductor field-effect transistors (MOSFET) has driven advances in computing capabilities. Following Moore's law and Dennard's scaling principles,[1,2] the semiconductor industry led the geometrical scaling era of transistors, which was followed by an essentially equivalent scaling era related to the increase of the effective velocity of electrons and holes in the channel, a decrease of the effective oxide thickness by means of high-*k* dielectrics, and the development of nonplanar fin channel field-effect transistors (FinFETS) to increase the transistor density. However, a strong slowdown of the Moore's law is expected to occur in the next few years because of the physical

G. Milano, L. Boarino
Advanced Materials Metrology and Life Sciences Division
INRiM (Istituto Nazionale di Ricerca Metrologica)
Strada delle Cacce 91, Torino 10135, Italy
E-mail: g.milano@inrim.it
M. Aono, K. Terabe
International Center for Materials Nanoarchitectonics (WPI-MANA)
National Institute for Materials Science (NIMS)
1-1 Namiki, Tsukuba, Ibaraki 305-0044, Japan
The ORCID identification number(s) for the author(s) of this article can be found under https://doi.org/10.1002/adma.202201248.

DOI: 10.1002/adma.202201248

U. Celano
IMEC
Kapeldreef 75, Heverlee, Leuven B-3001, Belgium
U. Celano
Faculty of Science and Technology and MESA+ Institute for Nanotechnology
University of Twente
Enschede, NB 7522, The Netherlands
T. Hasegawa
Faculty of Science and Engineering
Waseda University
3-4-1 Okubo, Shinjuku-ku, Tokyo 169-8555, Japan
M. Kozicki
School of Electrical
Computer and Energy Engineering
Arizona State University
Tempe, AZ 85287, USA

limitations for further transistor scaling.[3,4] In this scenario, emerging computing architectures beyond von Neumann are required to fulfill the ever-growing demand for data processing by exploiting emerging technologies, new device concepts, novel materials, and physical phenomena. Also, low-power hardware and computing paradigms are urgently required to decrease the ever-growing environmental cost and carbon footprint of our digital activities toward a sustainable and energy-efficient digital transformation.

Among all emergent technologies, memristive devices and memristive-based architectures represent promising candidates in the race toward alternative computing solutions with demonstrated impact in next-generation memory storage, in-memory computing, and bioinspired computing.[5,6] Although the existence of the memristor was theorized in 1971 by Prof. Chua,[7] the ideal concept of memristor was associated with resistive switching phenomena in nanoscale systems only in 2008 by Strukov et al.[8] This work resulted in accelerated interest in these nanodevices, but it is worth noting that resistive switching devices have been proposed as a new generation of nonvolatile memories even before being linked to the concept of memristor, as reviewed by Waser and Aono.[9] Recently, by taking advantage of the high scalability, high operational speed, and compatibility with metal–oxide–semiconductor (CMOS) technology both in terms of materials and processes, memristive devices have demonstrated storage applications, digital and logic applications, and neuromorphic-type data processing by emulating neuronal and synaptic dynamics for brain-inspired computing and for the hardware realization of artificial neural networks.[10–14]

Conventional memristive devices are two-terminal devices realized with a capacitor-like metal–insulator–metal (MIM) structure where an active material is sandwiched in between two metal electrodes, where functionalities rely on the dependence of the internal state of resistance and on the history of applied voltage and current.[11,15] Among the various physical mechanisms that have been exploited for the realization of these devices, redox-based memristive devices—nanoscale electrochemical systems where ionics is coupled with electronics—have risen to prominence.[9,16] Of particular importance is the fact that device functionalities are related to atomic reconfiguration phenomena that involve nanoionic processes.[9,17] In the case of electrochemical metallization memory cells (ECM), the device resistance can be modulated by transport of metal cations through the active material to form a nanosized atomic filament across the active insulating material connecting the two metal electrodes. This switches the device resistance from a high resistance state (HRS) to a low resistance state (LRS). In the case of valence change memory (VCM) devices, the switching mechanism is related to the migration of oxygen anions across the active material (which usually comprises a metal oxide) to form a substoichiometric nanosized conductive filament rich in oxygen vacancies. In this framework, device functionalities are determined by ion dynamics while electrons are exploited for probing the internal state of resistance.

Interestingly, when the conductive filament is shrunk down to the atomic scale, memristive devices exhibit quantum conductance related to ballistic electron transport through a mesoscopic constriction when its width is comparable to the electronic wavelength. In this case, the conductive filament forms a quantum point contact (QPC), a narrow constriction between two electrically conducting regions, where conductivity is quantized in terms of the fundamental unit of conductance $G_0 = 2e^2/h$.[18,19] Despite recent advances both in understanding fundamental physicochemical mechanisms underlying resistive switching events and in the realization of memristive-based computing architectures, a full appreciation of ballistic electron transport and quantum phenomena in memristive devices still represents a challenge. In this context, the potential of quantum effects in memristive devices is still rather unexplored.

In this work, we present a comprehensive review on memristive quantum devices where ionics is coupled with electronics to generate quantum conductance effects. An overview of pioneering work concerning the observation of quantum conductance phenomena in semiconductors and metals is first reported. Then fundamental electrochemical and physicochemical phenomena underlying ionic transport mechanisms related to the formation of atomic-sized conductive filaments in memristive devices are introduced. Following that is a discussion of electronic ballistic conduction transport properties in these nanoconstrictions acting as mesoscopic objects. In addition to an analysis of quantum effects related to resistive switching phenomena in low-dimensional memristive devices based on nanowires and 2D materials, quantum effects in conventional memristive devices are reported by discussing quantum mode splitting, quantum level stability, and random telegraph noise in these structures. Furthermore, an overview of physical and chemical analysis techniques and metrology for the investigation of nano constriction are reported. Due to the high scalability, high operational speed, and compatibility with CMOS technology and fabrication processes, memristive

S. Majumdar
VTT Technical Research Centre of Finland Ltd.
VTT
P.O. Box 1000, Espoo FI-02044, Finland
M. Menghini
IMDEA Nanociencia
Calle Faraday 9, Madrid E28049, Spain
E. Miranda
Departament d'Enginyeria Electrònica
Universitat Autònoma de Barcelona (UAB)
Barcelona 08193, Spain
C. Ricciardi
Department of Applied Science and Technology
Politecnico di Torino
C.so Duca degli Abruzzi 24, Torino 10129, Italy
S. Tappertzhofen
Chair for Micro- and Nanoelectronics
Department of Electrical Engineering and Information Technology
TU Dortmund University
Emil-Figge-Straße 68, D-44227 Dortmund, Germany
I. Valov
JARA - Fundamentals for Future Information Technology
52425 Jülich, Germany
E-mail: i.valov@fz-juelich.de
I. Valov
Peter-Grünberg-Institut (PGI 7)
Forschungszentrum Jülich
Wilhelm-Johnen-Straße
52425 Jülich, Germany

devices with controllable atomic-sized conductive filaments represent not only suitable platforms for the investigation of quantum phenomena but also for the realization of integrated quantum devices and architectures working in air and at room temperature.[18,19]

2. Conductance Quantization in Gate-Voltage-Controlled and Atom-Sized Point Contacts

In the late 80s, it was observed that the conductance of small constrictions in a 2D electron gas (2DEG) is quantized in units of G_0 when the diameter of the constriction is varied.[20,21] This is a consequence of the discrete number of modes or channels contributing to the overall conductance determined by the ratio between the channel width and the electron wavelength, as described by the Landauer formula (see ref. [22]). Interestingly, the optical analog of quantized conductance was then observed few years later by considering the transmitted power of light through a slit of variable width.[23] An important aspect is that the Landauer formalism describing quantization of conductivity in a point contact is not restricted to 2DEG systems only but can be generalized to any constriction where the lateral size of the constriction is comparable to the electron wavelength. Since the quantum of conductance involves constants of nature only, the quantization of ballistic electron transport is expected to occur both in semiconductors and metals.

Due to the large Fermi wavelength, a quantum point contact in a semiconductor is essentially a mesoscopic object. **Figure 1**a shows a schematic representation of a semiconductor-based device for the experimental observation of quantum conductance phenomena. A 2DEG is formed at the interface of the heterojunction and the point contact is created via a negative voltage applied to the top gate electrodes, while transport measurements are performed by attaching contacts at the two ends of the device.[24] The width of the constriction depends on the magnitude of the gate voltage, resulting in quantum steps of conductivity as a function of the control variable. Conductance quantization in semiconductors, firstly reported in a 2DEG formed at the interface of GaAs and AlGAs heterostructures,[20,21] was then reported at interfaces of various oxide insulators[25,26] as well as in graphene.[27]

The Fermi wavelength in metal is of the same order of magnitude as the atomic separation and the QPC must therefore be of atomic dimensions, as schematized in Figure 1b. As a consequence of the atomic size constriction, the level spacing in metallic point contacts is considerably larger so that conductance quantization can be observed at much higher temperatures (room temperature) with respect to semiconductor mesostructures where these effects are usually observable at a temperature lower than few Kelvin, as detailed in next sections.

In order to create metallic contacts with atomic-scale control of the distance, the technique of mechanically controllable break-junctions has been widely reported. This involves mechanically breaking a metallic wire in a vacuum at low temperature and then bringing the two pieces back into contact by means of piezoelectrical elements designed for the precise control of the distance in between them.[28] By exploiting this technique, conductance quantization has been reported in a wide range of metallic wires including Na, Au, Cu, Pb, Al, and Nb.[29,30]

Metallic QPC can be achieved also by means of a scanning tunneling microscope, where the point contact can be realized as the tip is pressed against a metallic surface.[31–33] By exploiting scanning tunneling microscopy (STM) in conjunction with electron microscopy, Ohnishi et al.[34] reported direct observation of the relation between quantum conductance and atomic structure of the metallic constriction. In their work, quantum steps of conductance were reported by withdrawal of the STM tip, as shown in **Figure 2**a. Transmission electron microscopy (TEM) images shown in Figure 2b illustrate the morphology of the gold strand at conductance steps A (left panel) and B (right panel), showing a dark line connecting the gap between the tip and the substrate. By analyzing the intensity profiles perpendicularly to bridges and according to electron microscopy imaging theory, the authors concluded that the $2G_0$ value observed at

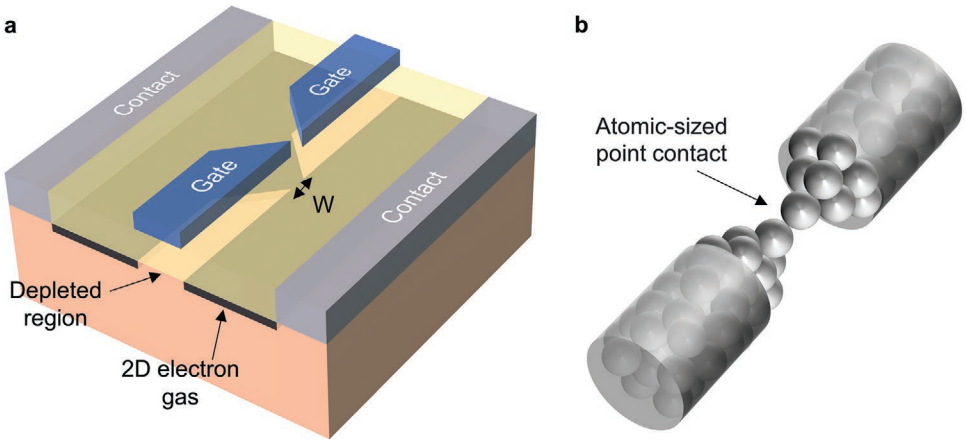

Figure 1. Quantum conductance phenomena in semiconductors and metals. a) Schematic representation of a semiconductor-based device showing conductance quantization, where a 2DEG is formed at the interface of a heterojunction. The quantum point contact is realized by applying a negative voltage to the gate electrodes while measuring transport properties through contacts to the 2DEG at either side of the constriction. The constriction width (W) can be varied by means of the applied gate voltage. b) Schematic representation of a metallic-based device where conductance quantization can be observed when the metallic contact is of atomic dimensions.

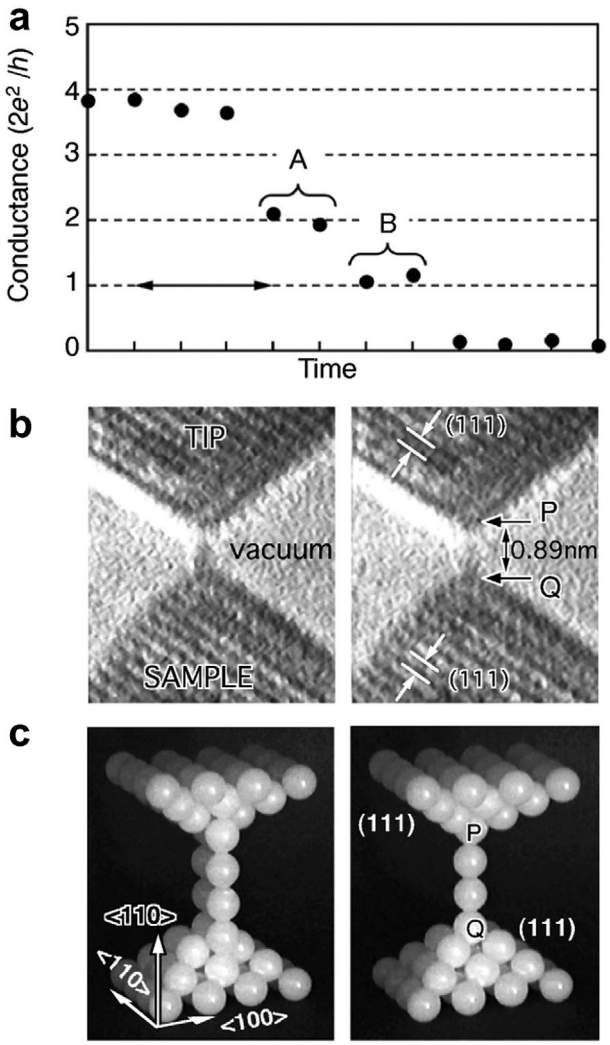

Figure 2. Quantum conductance effects of a single and a double strand of gold atoms. a) Conductance quantization observed by withdrawing the tip from the sample. b) Electron microscopy images of gold bridges obtained simultaneously with the conductance trace reported in (a). The electron images at step A and B are reported in the left and right panels, respectively. c) Schematization of metallic bridges with two rows of atoms at step A (left) and one row of atoms at step B (right). a–c) Adapted with permission.[34] Copyright 1998, Springer Nature.

step A is related to the presence of two rows of Au atoms while the single unit of conductance observed in step B arises from a single row of atoms as shown schematically in Figure 2c.

In all experiments based on break-junctions and STM tips, mechanical positioning systems are required to achieve the atomic point contact. These mechanical positioning systems, which usually require feedback control circuitry and/or piezo devices, hinder the possibility of the realization of large complex systems and architectures of integrated devices based on these quantum conductance phenomena. As an alternative, nonmechanical methods based on electrochemical techniques have been reported as a viable solution for the realization of nanoconstrictions with quantized conductance levels. As an example, Li and Tao[35] reported the realization of metallic constrictions with conductance quantum levels by means of electrochemical deposition/dissolution of a Cu nanowire between a metallic electrode and a STM tip, where the width of the nanowire was controlled by the applied electrical potential. Also, nanowire constriction with quantized conductance levels can be realized by electrochemical etching a narrow portion of a metallic wire, where the electrochemical potential regulates the etching or deposition of atoms onto the wire.[36]

Solid-state electrochemical reactions were reported by Terabe et al.[37] for the realization of atomic point contacts. In their work, a Ag_2S mixed ionic and electronic conductor is exploited as electrode and placed at a distance of about 1 nm from a counter Pt electrode substrate. By applying a positive voltage to the Ag_2S electrode with respect to the Pt electrode, migration of Ag^+ ions towards the Pt electrode followed by electrocrystallization was observed to occur, forming an atomic bridge of silver atoms connecting the two electrodes as shown in **Figure 3**a. By properly adjusting the electrical stimulation conditions, these Ag nanobridges exhibit quantum conductance. Interestingly, the formation of these conductive filaments was observed to be reversible, since an opposite voltage polarity causes ionization of Ag atoms of the conductive bridge that dissolve again in the Ag_2S bulk causing the shrinking and eventual breaking of the atomic bridge. In this fashion, the atomic point contact can be controlled simply by applying a voltage bias in between the electrodes without the need of any mechanical positioning system. By exploiting this working principle, Terabe et al.[38] reported the so-called atomic-switch devices working in air at room temperature where the internal state of resistance can be programmed in stable and well-defined quantum levels by means of electrical stimulation. These electrochemical phenomena underlying the formation/annihilation of a conductive bridge in the nanogap of atomic switches have been subsequently exploited for the realization of resistive switching and memristive devices. In case of resistive switching and memristive devices, the formation/annihilation of a conductive

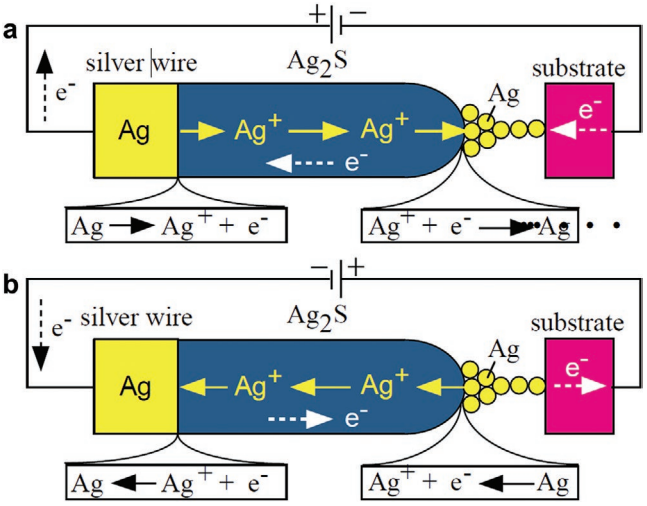

Figure 3. Quantum point contact realized by electrochemical reaction. The schematization of formation (a) and annihilation (b) of the atomic point contact obtained by applying a voltage difference between a mixed ionic and electronic conductor (Ag_2S) and a counter electrode substrate in a gap-type atomic switch. Adapted with permission.[37] Copyright 2001, Riken.

filament bridging the two metal electrodes occurs across the insulating matrix, turning the device from a high resistance state to a low resistance state and vice versa under the action of an applied electric field, as described in Section 3.

3. Electrochemical Formation of Nanosized Filaments

3.1. Working Principles of Resistive Switching Mechanism

Resistive switching phenomena are the foundation of memristive devices. Different criteria can be adopted to classify the variety of memristive devices reported in the literature. They can be systemized as: i) unipolar or bipolar, depending on the switching polarity; ii) filamentary or non-filamentary, depending on whether a filament short circuits the electrodes or involves a surface area/volume effect; iii) gap- or gapless-type, depending on whether a vacuum gap develops between one of the electrodes and the solid electrolyte or not; and iv) ReRAM (redox-or ferroelectric-based), PCM (phase change), MRAM (magnetic-based), STT-RAM (spin transfer torque), eRAM (electronic-effects-based) or NRAM (van der Waals forces based), depending on the physical phenomena responsible for the switching mechanism.[39] Each of the memristive device type shows strengths and weaknesses depending on the particular field of application and operation conditions. Formation and rupture of atomic point contacts and quantum effects are most frequently reported for filamentary type redox-based memristors (ReRAMs), which can be additionally split into electrochemical metallization cells (ECM), valence change memories (VCM) and thermochemical cells (TCM). Considering their functionalities and reliability, ECM and VCM devices are largely favored. In both type of cells, quantum conductance steps were observed.[18,38,40,41] To better understand this phenomenon it is necessary to understand in more detail the physical mechanism of the filament formation and the forces acting upon the filament structure, as discussed in the following.

ECM cells denoted also as conductive bridge RAMs (CBRAM) and/or programmable metallization cells (PMC) rely on the electrochemical formation (deposition) and rupture (dissolution) of a metallic filaments that short-circuit (SET) or disconnect (RESET) the device, defining the low resistive state (LRS or ON) and high resistive state (HRS or OFF) of the device, respectively. ECMs consist of: i) an electrochemically active electrode that can be Ag, Cu, Ni, Fe, etc. which can be oxidized by applying a positive voltage on it; ii) a switching film—it can be an oxide, a higher chalcogenide or a single-element material, e.g., Si (typically amorphous), that allows ions to be transported and iii) an inert counter electrode (metals such as Pt, Ir, etc, and compounds, e.g., TiN, ITO, etc.). Nevertheless, the definitions for active and inert metals are somehow blurred as even noble metals such as Pt, Pd, Ru, and Au were demonstrated to actively participate in the filament formation processes under specific conditions.[42–45] **Figure 4**a schematically shows the individual steps of the ECM mechanism as well as the corresponding current–voltage (*I–V*) characteristics. The processes leading to the filament formation under the applied bias shown in Figure 4a are: 1) redox reaction at the active electrode (oxidation), which provides metal cations into the switching matrix; 2) migration/diffusion of the ions towards the counter electrode, 3) nucleation/filament formation, and 4) filament growth.

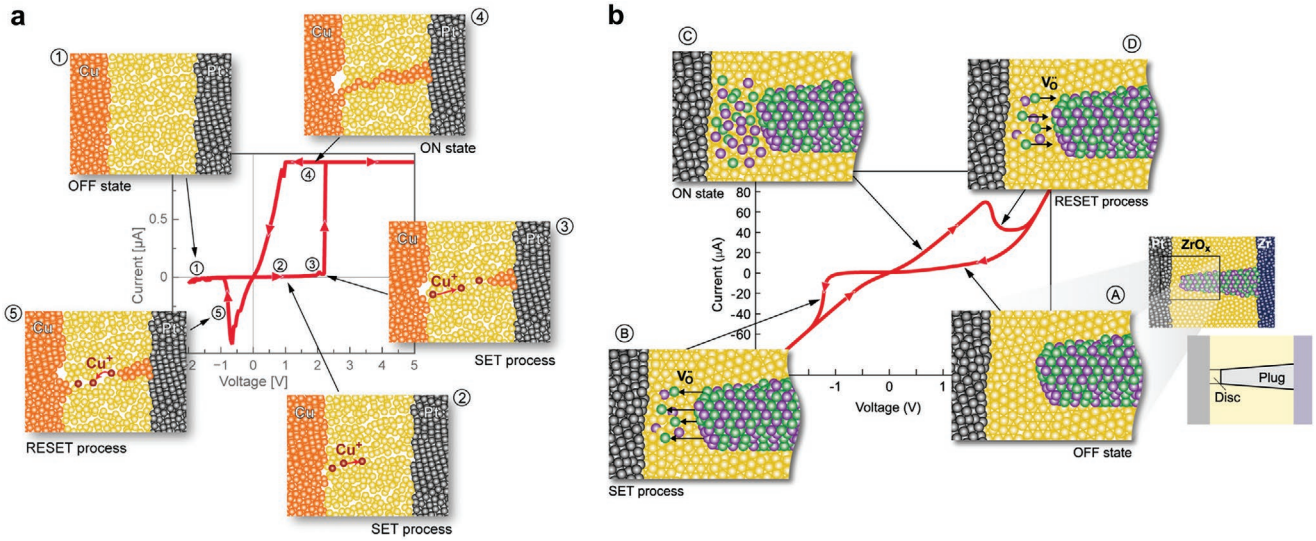

Figure 4. Working principle of ECM and VCM cells. a) Schematic representation of the processes during *I–V* sweep including formation and dissolution of a metallic filament in electrochemical metallization memories (ECM). The current saturation is due to the set current compliance (here 1 μA) used to prevent irreversible cell damages once the filament is formed. The value for the current compliance is chosen depending on the particular electrochemical system. It is also used to adjust the ON resistance (multilevel switching). The higher the current compliance the lower is the ON resistance. Using different current compliances the ON resistance can be varied by orders of magnitude. Reproduced with permission.[56] Copyright 2013, Wiley-VCH. b) Schematic presentation of the operation principle and related *I–V* characteristic of a VCM cell. Pt-electrode is serving as a Schottky electrode with high work function; Zr is the ohmic electrode and ZrO_2 is the switching film. The device is SET to ON state within the disc. The undesolved filament behind is denoted as a plug. Ⓐ is the OFF state, Ⓑ represents the SET and Ⓒ the ON state. The RESET process is given in Ⓓ. Reproduced with permission.[39] Copyright 2012, Wiley-VCH.

The dissolution of the filament occurs at reverse applied bias (step 5) and is also electrochemical in nature. Factors such as counter electrode reaction,[46] presence of moisture,[47,48] type of matrix, presence of doping/impurities,[49] and bond strength between mobile ions and surrounding matrix[50] are essential factors found responsible for the reliable operation of the device. Details of ECM fundamentals and the individual factors influencing the physicochemical processes described above can be found in the literature.[51–53]

VCM cells, denoted also as OxRAM, also rely on redox reactions. They consist of an ohmic electrode (e.g., Ti, Hf, Ta, or similar metal with high affinity to oxygen), a switching film (typically an oxide) and an inert electrode with higher work-function compared to the oxide (Schottky electrode). Here the ON and OFF states are a consequence of the Schottky barrier at the interface between the filament tip and the electrode. A schematic representation of these processes is provided in Figure 4b. In contrast to ECM, the filament is not completely dissolved during the RESET but remains largely intact (plug) during SET/RESET operations. Switching is triggered by ion movement and related redox reactions within a tiny disc (about 2–3 nm in diameter) between the partial filament/plug and the opposing electrode. In VCM, the main mobile species was originally supposed to be oxygen ions (or ion vacancies, using defect chemical terminology), but cations were also found to be part of this process.[54,55] The contribution of cations increases in the case of field-enhanced transport conditions as the oxidation number of the ions is in the exponential term of the equation for field-accelerated migration.[56] In the switching process, the exchange of oxygen (atoms/ions) between the ohmic electrode and switching film is also an important prerequisite for reliable operation. The ohmic electrode is in that respect electrochemically active and its electrochemical oxidation rate and absorption (oxygen scavenging) capacity need to be considered. The process can be seen as similar or even identical to the well-known electrochemical oxidation of metals, being an established approach for oxide thin film formation on metal surfaces.

In both ECM and VCM devices filaments are formed, whose diameter is considered to vary between a few nanometers up to several tens of nanometers.[57] The exact shape and morphology are determined by the driving forces (voltage, current), local conditions (temperature, environment), and physical/mechanical compressive/elastic forces (given by density and/or crystallinity of the switching film). The filament dynamics (formation, growth, stability) are complex and, due to the small size and related instabilities, are not easily assessable. Nevertheless, it has been shown that the shape of the filaments and even the growth direction depend on the combination of two factors, namely the electrochemical reaction rate and the mobility of the ions within the switching medium as schematized in **Figure 5**.[45] In the case where both reaction rate and mobility are high (case a), the growth proceeds from the cathode towards the anode and the filament exhibits a nearly conical shape. When both mobility and reaction are slow, a reverse growth mode occurs, in which the core filament develops from the anode toward the cathode via a mechanism based on bipolar electrode effects (case b). For the case in which the reaction is fast but the mobility low (case c), the bipolar electrode effect can be observed and monolithic filaments are rarely seen. Instead, when the mobility is high but the electrochemical reaction is slow (case d), the growth direction is preserved but the shape is more like tiny whiskers. Thus, according to these observations, it could be possible to predict or in some cases control the shape and size of the filaments by varying with the electrochemical reaction rate and the ion mobility.

The processes of formation and dissolution of the filaments often proceed through a stage that results in quantum point contact formation. After the first demonstration of this effect by Terabe et al.[38] for gap-type atomic switches (details in Section 1), further studies delivered more information for this process also in gapless-type devices.[40,58] Depending on the time of application of the voltage/current, the filament can be completed or just partially formed. During the formation process and after the applied field is switched off, different

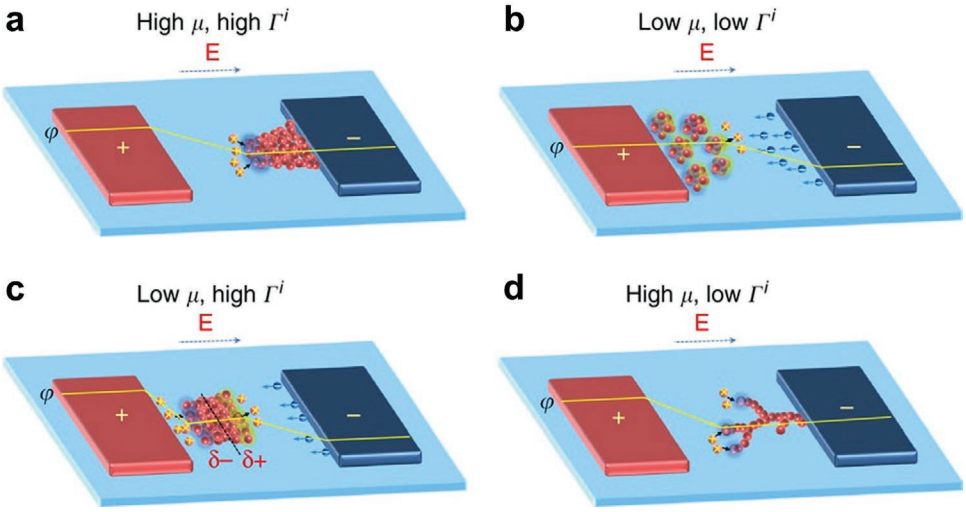

Figure 5. Mechanisms of filament growth. The shape and direction are determined by the electrochemical reaction rate and mobility. a) High mobility and reaction rate; b) low mobility and low rate; c) low mobility but high reaction rate; and d) high mobility and slow electrochemical reaction rate. Reproduced with permission.[45] Copyright 2014, Springer Nature.

supportive and destructive forces can act on the tiny filament as discussed in Sections 3.2 and 3.3.

3.2. Supporting Forces Acting on Nanofilaments

The strongest temporal supportive force driving filament growth is the applied voltage (through the electric field). The process starts with the filament nucleation described by the equation:[59]

$$\Delta G\left(N_{\mathrm{C}}\right)=N_{\mathrm{C}}\, e\,\Delta\varphi+\Phi\left(N_{\mathrm{C}}\right)+N_{\mathrm{C}}\varepsilon \tag{1}$$

where ΔG is the Gibbs formation energy of the critical nucleus, N_{C} the number of atoms constituting the critical nucleus, e the charge of the electron, $\Delta\phi$ the applied overvoltage, $\Phi(N_{\mathrm{C}})$ the specific free surface energy of the critical nucleus and ε the strain energy per atom.

Initially, the change in Gibbs formation energy must not be necessarily negative (i.e., leading to nucleation), the additional energy contribution $N_{\mathrm{C}}\varepsilon$ will inhibit the nucleation and the specific surface energy will try to keep its minimum. However, the applied voltage $\Delta\phi$ supports this process (cathodic overvoltage is negative) and makes the formation of the critical nucleus feasible. After the formation of the critical nucleus, the growth will proceed limited by the charge transfer (Butler–Volmer) kinetics:

$$j=j_0\left[\exp\left(\frac{(1-\alpha)ze}{kT}\Delta\varphi\right)-\exp\left(-\frac{\alpha ze}{kT}\Delta\varphi\right)\right] \tag{2}$$

with j and j_0 being the current density and the exchange current density, respectively; α is the transfer coefficient, and z the number of exchanged electrons.

In certain cases, diffusion-limited kinetics is observed so that (2) reduces to:

$$j=j_{\mathrm{d}}\left(1-\frac{kT}{ze}\Delta\varphi_{\mathrm{d}}\right) \tag{3}$$

which can also be formulated for field acceleration conditions as:

$$j_{\mathrm{d}}=2zecaf\exp\left(-\frac{\Delta G_{\mathrm{d}}^{\neq}}{kT}\Delta\varphi\right)\sinh\left(\frac{aze}{2kT}E\right) \tag{4}$$

where j_{d} denotes the diffusion determined current density, a the mean ion jump distance, f the attempt frequency, $\Delta G_{\mathrm{d}}^{\neq}$ the jump activation barrier height, c the ion concentration, and E the applied electric field. The combination of these factors (Equations 2–4) leads to the different growth modes and filament shapes as shown schematically in Figure 5.

Once formed, the filament is not necessarily uniform in shape and thickness. Thinner regions, that are potential weak points which lower the integrity of the filament, can often exist. However, a self-preserving mechanism can counteract such weaknesses to a certain extent. Metal filaments, with few exceptions, are in general subject to oxidative/corrosive effects. In many cases, however, the product of this corrosion can have protective functions, especially in the case of formation of dense layers, blocking further ion and/or electron transport (**Figure 6**a).

In case of application of a voltage across the filament (e.g., during read out or even "refresh" operations) Joule heating may occur, and the temperature increase will mainly affect the narrowest regions. Local increase of the temperature will shift the local electrode potential to more positive values and make deposition of metal atoms in these places preferential (Figure 6b). Note that this is a classical (not quantum) effect that is not expected to occur in the quantum point contact itself but that can take place in thicker filament regions where conduction is not ballistic.

An electric field gradient can also be formed in tiny restrictions, leading to movement of atoms in the direction oppose to the gradient (Figure 6c) leading again to a self-healing effect. Such effects have been already reported in the literature.[45] Again, this is not the picture for an ideal ballistic constriction in which in principle thermalization always occurs outside the region of interest.

3.3. Destructive Forces Acting on Nanofilaments

The supportive mechanisms described above are counteracted by certain destructive forces, which act to dissolve the filament. The oxidative/corrosive influence caused by the surrounding matrix (switching film) and the local environment (e.g., oxygen and moisture) lead to the removal of atoms and/or the formation of local corrosive conditions which break the filament (Figure 6d). Of considerable importance is the corrosive influence of moisture (H_2O). Corrosive galvanic elements can also appear at points of increased mechanical stress due to matrix-filament interactions (Figure 6e). The local corrosive elements will target the narrow regions of the wires, diminishing or eliminating the self-healing effects. The smallest sections of the filament will experience an excess in surface energy, which can also result in instabilities and/or destruction of these regions, breaking the integrity of the filaments (Figure 6d). Incomplete and/or disrupted filaments experience, in addition to corrosion, another destructive influence due to a nanobattery force,[60] namely the Gibbs–Thomson effect (Figure 6f).

$$\Delta\varphi_{\mathrm{GT}}=-\frac{\mu^{\mathrm{micro}}-\mu^{\mathrm{nano}}}{ze}=-\frac{2\gamma}{zer}V_{\mathrm{m}} \tag{5}$$

Here γ is the surface free energy, r the radius of the particle, V_{m} the molar volume, and μ the chemical potential of the nanofilament metal. Finally, the application of an anodic voltage to the filament could represent a strong driving force for its partial or complete dissolution. In addition, another driving force is related to the wind force arising due to the motion of electrons that transfer to atoms a momentum that is proportional to their velocity. This may lead to kicking-off of atoms and breaking the junction.

4. Ballistic Transport in Nanosized Filaments

Electron transport phenomena occurring in narrow constrictions such as nano and atomic-scale filaments in memristive

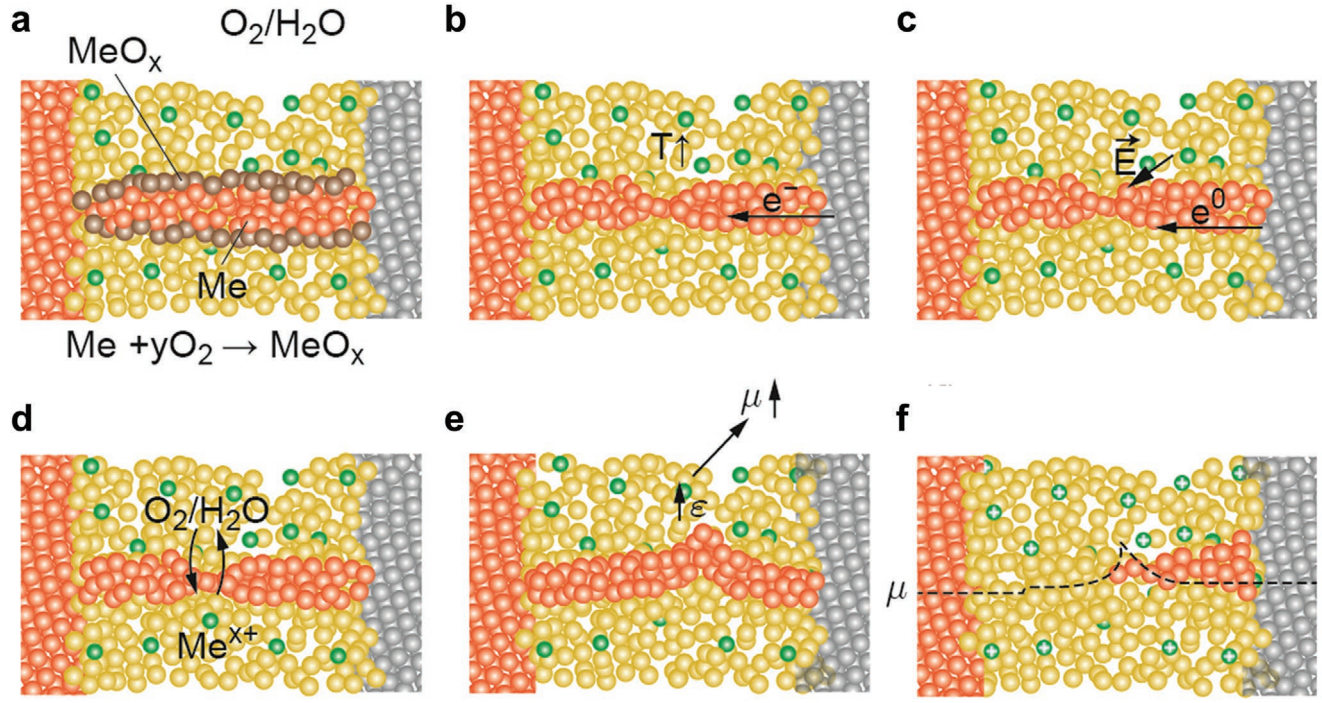

Figure 6. Schematization of supporting and destructive forces acting on electrochemically formed nanofilaments. a–c) Schematization of supportive forces acting on nanofilaments including: a) corrosion effects, b) Joule heating effects, and c) electric-field-gradient-driven supportive forces. d–f) Schematization of destructive forces acting on nanofilaments including: d) oxidative/corrosive influence of the surrounding matrix (switching film) and local environment (e.g., oxygen and moisture) leading to dissolution of atoms and/or formation of local corrosive elements breaking the filament, e) corrosive galvanic elements that can appear at points of increased mechanical stress due to matrix–filament interactions, and f) the Gibbs–Thomson effect.

devices can be viewed as a scattering or transmission experiment with modes, such as those occurring in electron waveguides.[61] Accordingly, understanding the role played by the geometrical and physical length scales involved in the system under study is essential to tackle the observed phenomenology and the corresponding device behavior.[62,63] As mentioned in previous sections, structures in which the electronic phase-coherence length L_ϕ, a measure of the distance over which quantum coherence is preserved, is of the same order of magnitude as the characteristic system size L but much larger than the Fermi wavelength λ_F are called mesoscopic systems. Phase coherence can be lost by electron-electron and electron–phonon interactions.[64] Since in many constricted systems the coherence lengths are hard to determine, electron transport in mesoscopic devices is often placed under the more general umbrella of one of the many faces of quantum transport theory.[65] Depending on the relation between the elastic mean free path of the electrons l, a measure of the distance between elastic collisions with static impurities, and the system size L, transport is often referred to as ballistic ($l >> L$) or diffusive ($l << L$). Typical values for Ag, Cu, and Au, are $l \approx$ 53.3, 37.7, and 39.9 nm, respectively.[66] The regime in between ballistic and diffusive is sometimes called quasi-ballistic. In the ballistic regime, the main topic of this paper, the electron momentum is considered to be conserved and only affected at the two ends of the structure, where thermalization is allowed. Momentum relaxation can indeed occur inside real structures because of inelastic interactions and this can be viewed as a localized potential drop along the system under study.[64] In the case of long and narrow constrictions, the conducting system is called a quantum wire, which can be treated as a 1D problem when the condition $W < L_\phi$ is satisfied. Additionally, if W is of the order of $\lambda_F/2$, the structure behaves as a monomode conductor exhibiting a resistance with value $R_0 = G_0^{-1} \approx 12.9\ \mathrm{k}\Omega$. In the following paragraphs, the theoretical framework for describing the conductance quantization provided by the Landauer–Büttiker (LB) theory of conductance is presented.[67,68] The LB formulism treats transport in constricted systems as a transmission problem for electrons close to the Fermi energy level. For the sake of brevity, the classical limit which arises from solving Poisson's equation for narrow circular constrictions (Maxwell approach)[69] and the semiclassical limit for small ballistic contacts (Sharvin conductance)[70] will be skipped.

To understand quantized conductance effects in 1D systems we can consider two electrodes A and B separated by a narrow constriction of length L and width W (see **Figure 7**a) in which phase-coherence is preserved. The electrodes behave as ideal electron reservoirs in thermal equilibrium with well-defined temperatures. Inelastic scattering is restricted to these reservoirs only. In the case of experiments based on break-junctions and STM tips, A and B are pulled apart by means of a mechanical force. This elongation leads to the rupture of the individual nanocontacts that form the atomic bridge so that the constriction becomes narrower as the electrodes retract. This is a major difference with respect to semiconductor constrictions in which the bottleneck size is gradually modulated by a control gate voltage. In memristive devices, the constriction is defined by the narrowest part of the filament formed by ions or vacancies that links both metal electrodes.

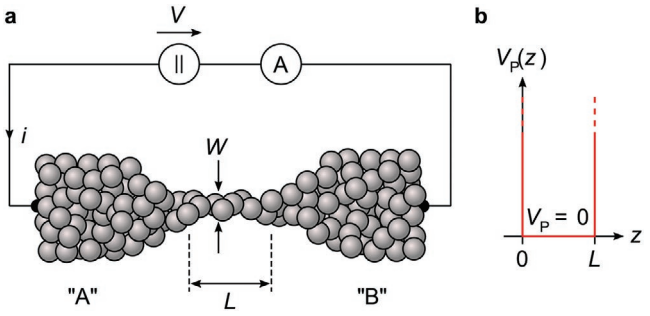

Figure 7. Ballistic electronic transport in a mesoscopic system. a) Schematic of two conductive reservoirs A and B connected by a constriction with length *L* and width *W*. b) Potential energy $V_P(z)$ of a particle in a 1D box.

Assuming ballistic transport in the constriction, the total current that flows through the structure can be calculated as the summation of the currents i_j transmitted by each channel *j*. Here, the term channel relates to the available conduction modes (sub-bands) in the constriction. Within this approximation, no mixing among channels is allowed. According to the LB approach, the current i_j reads:

$$i_j = \frac{T_j}{R_j} env \tag{6}$$

where *e* is the electron charge, *n* the electron concentration, and *v* the velocity of the electrons in the 1D system. T_j and R_j are the transmission and reflection coefficients for channel *j*. The mode splitting which arises from the electron wavefunction confinement effect is $\Delta E = \pi^2\hbar^2/(2m\lambda_F^2)$. Here, $\lambda_F = 2\pi/k_F$ is the Fermi wavelength and k_F the Fermi wave-vector. Typical values for λ_F are 0.52 nm for Au and Ag, 0.46 nm for Cu, and 50 nm for a 2D electron gas (2DEG) in GaAs. In general, quantum conductance levels can be observed if $\Delta E >> kT$, *k* being the Boltzmann constant and *T* the absolute temperature. Accordingly, quantum conductance effects in Au, Cu, or Ag can be observed at room temperature ($\Delta E \approx 1\,\text{eV} \gg k_B T \approx 26\,\text{meV}$). On the contrary, 2DEG-experiments require much lower temperatures (typically $T < 4$ K). More in depth, it can be shown that the number of quantum channels in a constriction can be linked to the number of valence orbitals of the atoms forming the conductive bridge.[71]

According to quantum statistics, the electron concentration *n* can be expressed as:

$$n = \int_{E_C}^{\infty} f(E)\cdot D(E)\,dE \tag{7}$$

where E_C is the energy corresponding to the bottom of the conduction band, $D(E)$ the density of states, and $f(E)$ the Fermi–Dirac distribution. Assuming that only a small range of energies around the Fermi level E_F plays a significant role for conduction, Equation (7) can be simplified as:

$$n \approx \frac{1}{2}\cdot D(E)\cdot E \tag{8}$$

The density of states is calculated as follows. Let us consider the case of a particle in a box with infinite walls such as that illustrated in Figure 7b. The particle (electron) can be found in the region $0 < z < L$. According to the 1D time-independent Schrödinger equation, the wavefunction $\psi(z)$ associated with the particle must obey:

$$-\frac{\hbar^2}{2m}\frac{d^2\psi(z)}{dz^2} + V_P\psi(z) = E\psi(z) \tag{9}$$

where *E* is the energy of the particle, *m* its mass, and $\hbar = h/(2\pi)$ is the reduced Planck constant. A solution to Equation (9) in the form of $\psi(z) = \sqrt{2/L}\sin(kz)$ (with the wave number $k = n\pi/L$, *n* being an integer) can be derived using the boundary conditions $\psi(0) = \psi(L) = 0$. With these boundary conditions, the relationship between the kinetic energy and the wave number *k* for the particle inside the box can be established as:

$$E = \frac{\hbar^2 k^2}{2m} \tag{10}$$

From Equation (10), it follows that in *k*-space all points located a distance k^2 apart from the origin have the same energy. These points form a shell of equal energy with radius *k*. The volume of this subspace is $V_k = 4\pi k^3/3$ in 3D, $V_k = \pi k^2$ in 2D, and $V_k = 2k$ in 1D. Transforming the problem of a particle in a box from real to *k*-space, the *k*-vectors also form a volume $\Omega_k = k_x \cdot k_y \cdot k_z = (2\pi/L)^3$ in 3D, $\Omega_k = (2\pi/L)^2$ in 2D, and $\Omega_k = 2\pi/L$ in 1D. Now, taking into account a factor 2 for the spin-degeneracy, we can calculate the ratio between V_k and Ω_k for a 1D system as:

$$N(k) = 2\cdot\frac{V_k}{\Omega_k} = 2\frac{2k}{2\pi/L} = \frac{2kL}{\pi} \tag{11}$$

From Equation (10), $k = \sqrt{2mE}/\hbar$, and since $N(k)dk = N(E)dE$ we find $N(E) = 2L\sqrt{2mE}/(\hbar\pi)$. Then, the density of states becomes:

$$D(E) = \frac{1}{L}\cdot\frac{dN(E)}{dE} = \frac{\sqrt{2m}}{\hbar\pi}\cdot\frac{1}{\sqrt{E}} \tag{12}$$

Substituting Equation (12) into Equation (7), we obtain:

$$n = \frac{1}{2}\cdot\frac{\sqrt{2m}}{\hbar\pi}\cdot\frac{1}{\sqrt{E}}\cdot E = \frac{1}{2}\cdot\frac{\sqrt{2m}}{\hbar\pi}\cdot\sqrt{E} \tag{13}$$

Now, considering that $v = \sqrt{2E/m}$ and $E = eV$, *V* being a small applied voltage, we find with the help of Equation (6):

$$i_j = \frac{T_j}{R_j}e\frac{1}{2}\cdot\frac{\sqrt{2m}}{\hbar\pi}\cdot\sqrt{E}\cdot\sqrt{\frac{2E}{m}} = \frac{T_j}{R_j}\cdot\frac{e}{\hbar\pi}\cdot E = \frac{T_j}{R_j}\cdot\frac{2e^2}{h}\cdot V \tag{14}$$

Since $G_0 = 2e^2/h$, the total current is then given by the summation over all channels *j*:

$$i = \sum_j i_j = G_0\cdot V\cdot\sum_j\frac{T_j}{R_j} = G_0\cdot V\cdot\sum_j\frac{T_j}{1-T_j} \tag{15}$$

To further simplify Equation (15), let's consider that all the channels are equivalent, that is:

$$I = G_0 \cdot N \cdot \frac{T}{1-T} \cdot V \tag{16}$$

where N is the number of available channels and T is the transmission probability. Now, following Imry's interpretation,[72] we consider the contact resistances (the resistances that arise between the reservoirs and the 1D structure associated with the mismatch in the number of conducting modes), so that:

$$\frac{1}{G} = \frac{1}{G_0 \cdot N} + \frac{1}{G_0 \cdot N} \cdot \frac{1-T}{T} = \frac{1}{G_0 \cdot N} \cdot \frac{1}{T} \tag{17}$$

which leads to the simple expression:

$$G = G_0 NT \tag{18}$$

or in terms of the current and voltage:

$$I = G_0 NTV \tag{19}$$

Equation (18) is the celebrated Landauer formula that connects conductance with transmission probability and which is the basis for understanding the physics of mesoscopic systems.[73] Before continuing, it is important to briefly point out the main limitations of the above development. As discussed in ref. [71], the LB approach is fundamentally a phenomenological theory that: i) relies on the scattering properties of the structure without establishing a clear link with the microscopic aspect of the problem, ii) does not account for self-consistency for the electrostatic potential, iii) only considers a fully quantum coherent transport process, and iv) does not include electron correlation effects. In this context, non-ideal factors including stress and filament geometry/nanostructure (see also Figure 6) can result in a deviation from the Landauer theory. Also, application of a finite bias voltage and finite temperatures requires a more in-depth analysis. Indeed, Equation (19) can be extended to the finite bias case by taking into account the energy dependence of T:[74]

$$I = \frac{2e}{h} \int T(E,V) \left[f(E - \beta eV) - f(E + (1-\beta)eV \right] dE \tag{20}$$

where the constant $0 < \beta < 1$ is the fraction of V that drops on the source side of the constriction. Following refs. [75, 76], if an inverted parabolic barrier of height Φ is assumed for describing the bottom of the first quantized sub-band at its narrowest point and the smearing of the Fermi functions at the electrodes is neglected (zero-temperature limit), the current becomes:

$$I(V) = \frac{2e}{h} \left\{ eV + \frac{1}{\alpha} \ln \left[\frac{1 + \exp\left\{\alpha\left[\Phi - \beta eV\right]\right\}}{1 + \exp\left\{\alpha\left[\Phi + (1-\beta)eV\right]\right\}} \right] \right\} \tag{21}$$

α is a parameter related to the longitudinal shape of the barrier and more specifically to the second derivative of the potential profile.[77] Equation (21) is valid for a single-mode ballistic conductor ($N = 1$). When the constriction is wide, Φ does not play any role ($T \approx 1$) and Equation (21) reduces to Equation (19). However, if the constriction is narrow ($T < 1$), Equation (21) results in an exponential dependence of the I–V characteristic. These two extreme cases have been identified with the LRS and HRS conduction modes in resistive switching devices, respectively.[78,79] Furthermore, following ref. [80], it was demonstrated that the LRS I–V characteristic can be approximated by the expression:[81]

$$I = G_0 \left(\beta \vec{N} + (1-\beta) \overleftarrow{N} \right) V \tag{22}$$

where $\vec{N}$ and $\overleftarrow{N}$ are the number of right- and left-going conduction modes, respectively. This is a consequence of the specific energy location of the top of the confinement potential barrier with respect to the quasi-fermi levels at the reservoirs. For symmetrical potential drops at the two ends of the constriction ($\beta = 1/2$), Equation (22) reduces to:

$$I = G_0 NV \tag{23}$$

where $N = \left(\vec{N} + \overleftarrow{N}\right)/2$. Notice that Equation (23) is formally equivalent to the Landauer formula, Equation (19). However, if the difference between $\vec{N}$ and $\overleftarrow{N}$ is an even number, Equation (23) predicts integer multiples of G_0, whereas if the difference between $\vec{N}$ and $\overleftarrow{N}$ is an odd number, half-integer multiples of G_0 are obtained. These are referred to as the linear and nonlinear conduction modes in quantum-point contacts, respectively, and have been reported many times in RRAM devices.[82,83] In this connection, it is worth emphasizing that caution should be exercised with the use of the term conductance quantization in RRAM devices:[18] as experimentally observed, only for simple s-electron metals the transmission probability for the conductance channels is expected to be close to integer values as expressed by Equation (18).[71,84] For this reason, observation of quantum steps in the conduction characteristics of RRAMs should be more appropriately considered to be in the quantum (rather than in the quantized) regime of conductance.[85] In this context, it should be remarked that in conventional QPCs half-integer quantization has been ascribed to spin polarization effects as well. However, it is important to emphasize that quantum effects in memristive devices differ from conventional QPC phenomena in the sense that the observed jumps of conductance in resistive switching devices are not the result of a pure electrical effect. Indeed, the jumps correspond to structural modifications of the filamentary pathway caused by the ion/vacancy movement. The fact that QPC in memristive devices does not result from a pure electronic mechanism is revealed when the applied voltage is decreased (without changing its sign) and the current does not follow the original path (hysteresis). This behavior does not occur in purely electronic conventional QPC systems where the I–V path remains always the same without showing a hysteretic behavior. As a consequence, even though polarization effects cannot be disregarded in memristive devices, the picture associated with the blocking of conducting states (because of the relative energy location of the barrier with respect to the injecting contacts) is suggested to be more plausible. In this framework, quantization of the conductance should be discerned from stepwise variations in the conductance that can arise from discrete atomic structures of the contact with limited numbers of accessible configurations, as detailed in refs. [85, 86]. True conductance quantization can be distinguished from discrete variations

in contact size by analyzing the characteristic sequence of conductance values arising from mode degeneracy.[29]

In spite of the limitations discussed above and the uncertainties, it is more than clear that Landauer's theory has achieved great success in the field of quantum transport providing a feasible explanation to a plethora of phenomena, including the occurrence of quantum effects in memristive devices.

5. Quantum Conductance Regime in Resistive Switching and Memristive Devices

Research on resistive switching memories started in the 1960s[87,88] but fell in popularity with the advent of solid-state memories based on floating-gate transistors[89] and flash memory.[90] In the 2000s, Flash scaling became a serious challenge,[91] and alternative concepts including resistive switching memories attracted large attention.[16,92–95] The observation of localized switching effects at the nanoscale[96] demonstrated the potential of resistive switches to be scaled down to almost atomic level (i.e., the lateral size of the filament). In these length scales, quantum conductance effects can play a dominating role during and after the resistance transition even at room temperature as previously discussed in Section 4.

5.1. Experimental Demonstrations

The first demonstration of quantum conductance effects in so-called gap-type resistive switches (atomic switch) was reported by Terabe et al. in 2001 and 2004.[37,38] The authors fabricated a microscale crossbar based on a silver wire as a bottom-electrode and a platinum top-electrode, where the top-electrode was separated from the bottom electrode by a thin-film heterostructure composed of Ag_2S and Ag. By applying an appropriate voltage between both electrodes, the Ag thin-film was dissolved in the Ag_2S layer, which eventually formed a 1 nm thick vacuum gap (hence the name gap-type atomic switch) between the Ag_2S and platinum layer. Upon bipolar voltage cycling, a nanoscale silver wire can be formed and erased in the vacuum gap, which modules the device conductance. **Figure 8**a depicts the sample structure and Figure 8b the device operation principle.[38,97] The authors observed the signature of quantum point conductance effects $\sigma = 2ne^2/h$ (where n is an integer number) upon tuning the device conductance at room temperature as reported in Figure 8c.

The vacuum gap allows the filament to be formed and erased independently (and thus without any morphological restriction and nano-mechanical stress) from any surrounding switching material. However, later on, conductance quantization effects were observed in conventional (gapless) resistive switching devices, including ECM[40,86] and VCM[98,99] devices.

For example, by considering ECM cells, by applying a current-sweep quantum conductance steps were observed in a Ag/AgI/Pt-based resistive switch as reported in **Figure 9**a. Similar quantum conductance behavior has been also observed for mixed-ionic conductors such as Ag_2S[86,100] (Figure 9b) and GeS_2,[101] and even oxides including SiO_2,[102–104] Ta_2O_5,[99,105] HfO_2,[106,107] $Zr_{0.5}$ $Hf_{0.5}O_2$.[108] Also, quantum effects with an ECM-type memristive mechanism have been reported in devices with an insulating matrix based on polymers,[109,110] amorphous carbon,[111] graphene nanoplatelets,[112] and natural acidic polysaccharides.[113]

In all cases, step-wise conductance changes were measured, which can be attributed to an integer multiple of the one atomic point contact conductivity $G_0^{-1} \approx 12.9\ \mathrm{k\Omega}$. However, the atomic point contact is in series to the bulk filament resistance R_F, which can be in the order of some hundreds of Ω to kΩ, and is thus in a similar range as G_0^{-1}.[40,102] This results in a deviation of the measured device conductance $G = (R_F + (nG_0)^{-1})^{-1}$ from the expected value nG_0. Also, due to statistical variations a conductance state histogram is usually obtained, as for example reported in Figure 9c where the conductance state was statistically evaluated by considering more than two hundred datasets obtained in different devices.[105] Note that in ECM cells also Coulomb-blockade effects have been reported when measured at low temperature.[114] Remarkably, Jameson et al.[101] demonstrated the programmability of quantum levels in $Ag/GeS_2/W$ cells produced in a foundry as part of a CBRAM memory chip, proving that memristive devices working in the quantum regime are scalable and manufacturable.

The first report of quantization effects in SiO_2 dates back to the late 90s, where Sune et al.[115] demonstrated experimentally and by simulations that the dielectric breakdown of SiO_2 films in MOS (metal–oxide–semiconductor) devices opens atomic-sized conduction channels acting as quantum point contacts. In a later work, Mehonic et al.[82] reported on conductance quantization effects in silicon oxide (SiO_x)-based valence change mechanism devices. In contrast to early studies on conductance quantization in CBRAM devices, Mehonic et al. reported on half-integer multiples of the one atomic point contact conductivity (Figure 9d). Following a previous paper by Miranda et al.,[81] the authors attributed the discrepancy of experimental findings in the literature reporting on either integer or half-integer values of G_0 to the chemical potential gradient across the conductive filament and the energy location of the confinement potential barrier with respect to the quasi-Fermi levels at the contacts. In CBRAM devices, the metallic filament may not allow a large chemical potential gradient to be maintained across the atomic point contact. Thus, the conductivity is driven by injecting electrons in the same energetic subband of the atomic-size constriction. For VCM devices, the filament formation is driven by oxygen-vacancies $V_O^{\cdot\cdot}$ and the filament is composed of a matrix of cations and $V_O^{\cdot}$, as previously discussed in detail in Section 3.1. Thus, the quantum point contact can maintain larger chemical potential gradients and the modes of the electrons driven across the atomic point contact fall in different energetic subbands. It can be shown that the latter can result in half-integer values of the one atomic point contact conductivity. Note that in an ideal quantum point contact there is no potential drop along the constriction and the potential drops occur mainly at the contacts, for this reason the structure can sustain large current densities. A potential drop in a quantum constriction occurs when phase relaxation is allowed or when a barrier or gap exists along the filament. Quantum conductance effects have now been observed at room temperature in various VCM-type devices (most showing half-integer values of G_0), including devices based on HfO_2,[98,116,117]

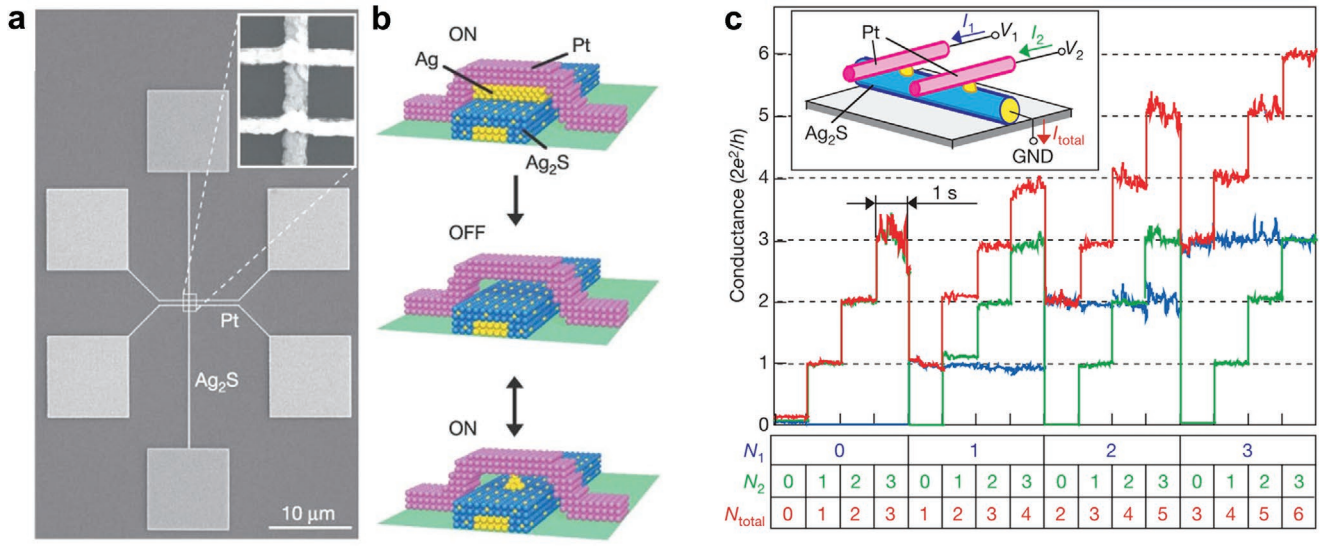

Figure 8. Quantum conductance effects in gap-type atomic switches. a) Scanning electron microscopy image of the crossbar sample structure consisting of two atomic switches. b) Operation principle of the atomic switch: the Ag layer separating Ag_2S and Pt is at first dissolved in Ag_2S, which eventually leads to the formation of a vacuum gap. Upon applying bipolar voltage signals across the crossbar, a nanoscale Ag filament can be formed in the gap. c) By applying voltage pulses (length 50 ms, voltages amplitudes of 200 mV from 0 to 1, 100 mV from 1 to 2, 80 mV from 2 to 3, and 260 mV from 3 to 0) the conductance of the atomic switches (blue and green) and the total conductance (red) is step-wise increased by integer multiple of the one atomic point contact conductivity $2e^2/h$. a–c) Reproduced with permission.[38] Copyright 2005, Springer Nature.

ZnO,[118] SiO_2,[119] CeO_x/SiO_2,[81] NiO,[120] TiO_2,[121–123] Gd_2O_3,[124] and Ta_2O_5.[125,126] The appearance probability of quantum point contact in VCM cells can be improved by optimizing the distribution of oxygen vacancies, as for example reported by hydrogen thermal treatment.[127] It is worth noting that the transition between quantum levels in resistive switching devices is

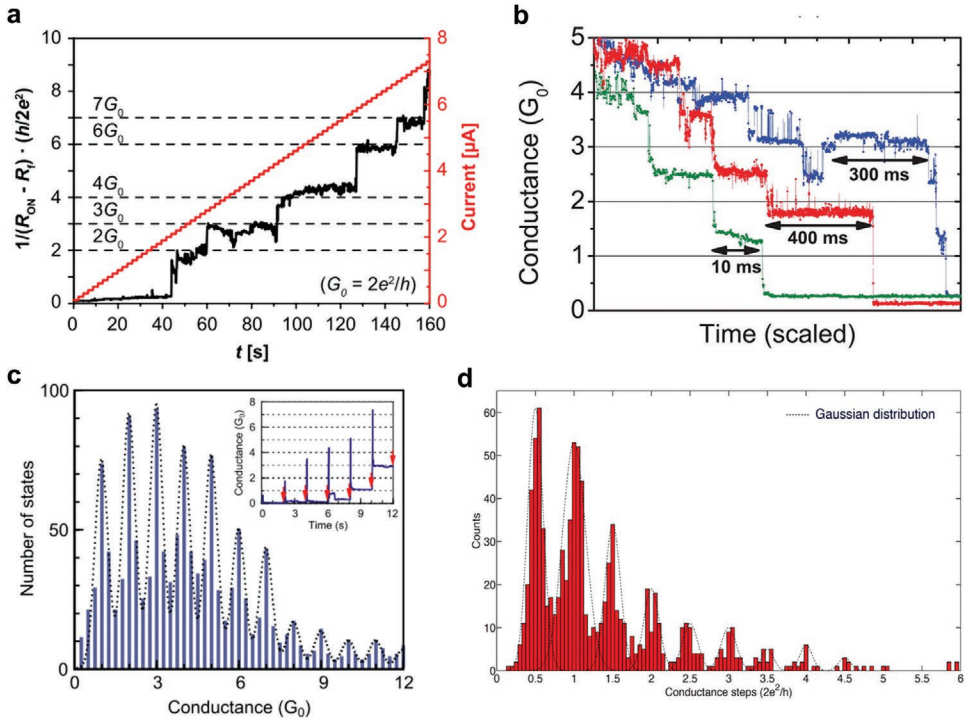

Figure 9. Conductance quantization effects in gapless resistive switchers. a) Step-wise increase of the filament conductance of a Ag/AgI/Pt resistive switch by using a current-sweep. Reproduced with permission.[40] Copyright 2012, IOP Publishing Ltd. b) Step-wise decrease of the filament conductance of a Pt/Ag_2S/Pt device upon reset. Reproduced with permission.[86] Copyright 2012, AIP Publishing. c,d) Histogram of conductance quantization effects for Ag/Ta_2O_5/Pt CBRAM-device (c) derived from voltage or sweep experiments and for a poly-Si/SiO_x/poly-Si VCM-type device (d). c) Reproduced with permission.[105] Copyright 2012, IOP Publishing. d) Reproduced with permission.[82] Copyright 2013, Springer Nature.

related to electrically induced morphological changes of the filament and, in this sense, quantum effects in these devices are more similar to break-junction QPC rather than 2DEG QPC. In this context, evidence of truly atomic-sized metallic filaments was reported by Török et al.[128] who reported the transmission probabilities of each individual conduction channel contributing to conductance, the so-called quantum PIN code, through superconducting subgap spectroscopy. Similarly, nonlinearities of current-voltage characteristics caused by superconductivity combined with transmission channel analysis and molecular dynamics were previously investigated by Schirm et al.[129] in a current-driven single-atom memory device based on a few-atom aluminum contact. In this context, the nature of stepwise variations of conductivity depends on the peculiar device configuration, employed materials, and operating conditions.

5.2. Quantum Level Stability and Random Telegraph Noise

In resistive switches, the conducting filament acts as a waveguide for electrons and provides ballistic transport between the electrodes, as discussed in Section 4. Three requirements need to be fulfilled in order to observe quantum conductance effects in resistive switches at room temperature. The first requirement is that quantum point contacts are structurally feasible, which is fulfilled by the nanoscale geometry of the filament. The second requirement is related to the thermal energy since quantum conductance effects can be observed when the energy of the quantum mode splitting is larger than the thermal energy (details in Section 4). The third requirement is related to the experimental conditions. Thermally induced fluctuations of even single atoms forming the quantum point contact[125,130] may not only affect the measured conductivity level but could also impede the observation of quantum conductance effects. Therefore, standard quantum point contacts must have a certain electrochemical and thermomechanical stability of at least some microseconds to seconds (depending on the measurement system's bandwidth) to be experimentally observable. Typical time scales in which stable quantum conductance levels are observed are in a time range between some hundreds of milliseconds[86] to some tens of seconds.[40,105] Deswal et al. reported on the importance of the formation conditions to set quantum conductance levels.[131] On the contrary, by precise limitation of the current compliance during current–voltage sweeping, the authors could observe conductance quantization effects with a stability of some hundreds of seconds in a $Al/Nb_2O_5/Pt$ VCM device. A similar stability has been demonstrated by Yi et al. for $Ta/TaO_x/Pt$ devices[125] and an even higher stability in the order of 10^4 s has been reported by Chen et al. for $Pt/HfO_x/Pt$[132] (**Figure 10**a). However, little is known on the fundamental thermomechanical or electrochemical processes controlling the atomic stability of the filament and in particular of the quantum point contact. Since resistive switches are based on nanoionic redox reactions, processes similar to those in (nano-) batteries[60] can affect or even dominate device behavior.[133] Based on these processes, 1D kinetic Monte Carlo simulations supported by experimental findings revealed an electrochemical stability of quantum conductance levels in the order of some tens of seconds for $Ag/SiO_2/Pt$-based ECM cells.[102] Though only limited studies in the literature report on the stability of quantum conductance effects, the general trend is that high stability is observed in particular for VCM-type devices. For example, quantum conductance levels with high stability and reproducibility have been reported by Hu et al. for TiO_2-based devices,[122] where the switching is dominated by migration of oxygen vacancies. The authors attribute the stability to reasonably robust conductive Magnéli-like nanophases. High stabilities reported by Deswal et al.,[131] Yi et al.,[125] and Chen et al.[132] have been all also observed in VCM-type switching devices. Another phenomenon that is linked to quantum-scale effects is the observation of sudden stochastic step-like transitions between two discrete current levels of resistive switches (Figure 10b). This effect is called random telegraph noise (RTN) and has been observed in various resistive switching devices.[134–136] RTN shows the signature of $1/f$-noise (where f is the frequency) and is also important for conventional semiconductor devices.[137–139] In memristive devices, RTN has been suggested as true random generators for providing high encryption security.[134,135] The $1/f$-noise signature can either originate from release and trapping of electrons in/from defects,[135,136,140] or atomic fluctuations (also termed as "ionic telegraph noise").[134,141] The latter is linked to the stability of the conductive filament (and the quantum point contact).

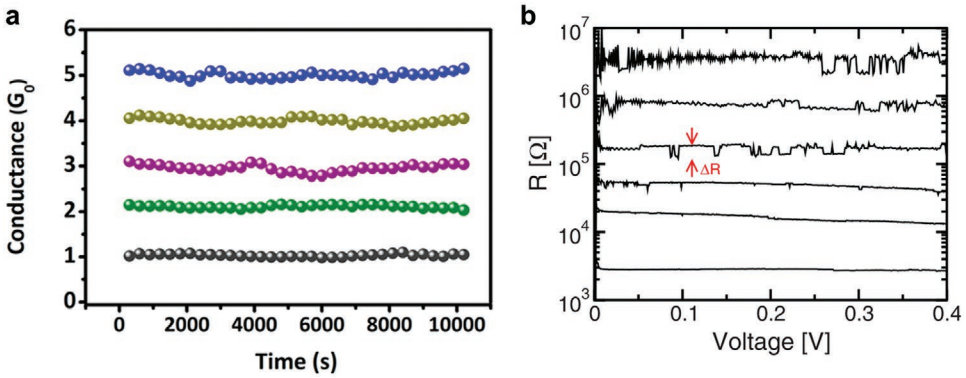

Figure 10. Quantum-scale effects in resistive switches. a) High stability of quantum conductance levels. Reproduced with permission.[132] Copyright 2019, American Chemical Society. b) Random telegraph noise in a NiO-based resistive switch. Reproduced with permission.[136] Copyright 2010, AIP Publishing.

5.3. Operating Modes

Mechanical breaking of macroscopic gold wires readily allows the observation of quantum conductance effects at room temperature. This has even been suggested as an experiment at high school or college undergraduate level.[142] In these experiments, a constant voltage is applied to a wire while the transient current is monitored using an oscilloscope. Upon pulling the two ends of the wire apart, the resistance change is recorded. Immediately before the wire is broken, quantum conductance effects are observed. The conductive path in a VCM-type or CBRAM-type resistive switch behaves like a nanowire and its resistance can be tuned in a regime where single atoms dominate the path's conductivity. Likewise, a constant voltage (typically some tens of mV to 100 mV) can be applied to a resistive switch to observe quantum conductance levels. This is called the constant-voltage mode and the reason for a conductivity change is the applied constant voltage resulting in an electrochemical stimulus.[58,105] The difficulty is that the applied voltage must not be to high otherwise the quantum conductance effect is too brief to be observed. However, if the applied voltage is too small, the conductance change time may be too long for the experiment. Therefore, dynamic sweeping experiments have been suggested. A related method to the constant-voltage mode is the voltage-pulse operation. In this case, voltage pulses (length ≈ µs to ms) with constant or variable amplitudes are applied followed by a long voltage pulse with a low amplitude to measure the device resistance.[105] This method allows the observation of several quantum conductance levels if the pulse length and amplitude are tuned appropriately. A straightforward experimental method is the voltage sweep method,[40,81,116,118,143] where a triangular voltage is applied to the device and the current is recorded simultaneously. This operation is identical to voltage-sweep experiments, which are commonly used for investigation of resistive switching effects. Here quantum conductance effects are observed during SET and RESET operations on the device. The difficulty is to find a voltage-step size that is small enough to probe as many quantum conductance steps as possible while keeping the overall measurement time at a moderate level. Instead of voltage sweeps, current sweeps can also be applied. The current-sweeping method is motivated by the electrochemical interpretation that the removal of single atoms from the narrowest part of the tip is related to a discrete charge for ionization of the atoms. By controlling the current and thus the charge, a high control of the atomic rearrangement is expected. In fact, using this method[102,40] several conductance levels can be observed, especially for systems where only single conductance steps are observed using the voltage sweep method. However, the difficulty here is to precisely control the current (nA to µA range with µs to ms response) otherwise the conductance steps cannot be recorded.

It appears that there is no dominating technique to probe conductance quantization effects and the right choice of the operation mode depends on the device (e.g., RC-time), material system (switching kinetics and electrochemical overpotentials), and experimental capabilities (bandwidth but also temperature, ambient, etc.).

5.4. Quantum Effects in Low Dimensional Memristive Devices

Despite sharing the same working principle of conventional stacked cells, memristive devices based on low dimensional materials can represent suitable platforms for easier localization and characterization of switching phenomena. More interestingly, memristive systems and architectures based on low-dimensional materials can be also explored for the realization of transparent, bendable unconventional architectures and neuromorphic systems.

5.4.1. 1D Materials

Memristive devices and architectures based on nanowires (NWs) have attracted increasing interest since the first experimental observation of resistive switching in a single NiO NW in 2008.[144] As bottom-up building blocks, the main advantages of 1D structures are their ultimate scalability, their high spatial localization of switching events, and their large surface-to-volume ratio that can be exploited to tune the electronic/ionic transport contributions.

Concerning single-NW-based devices, both ECM and VCM mechanisms of resistive switching have been reported in isolated metal oxide NWs (CuO, ZnO, TiO_2, NiO are the most common), which can be single crystal, polycrystalline or heterostructured.[145] A particularly effective configuration of ECM employs a single-crystal semiconducting NW between an electromigrating electrode (Ag or Cu) and an inert electrode (Pt).[146,147] In this case, the low concentration of defects in the crystalline NW reduces the ionic transport in the bulk, so that the conductive bridge formation and rupture are localized on the NW surface (**Figure 11**a). In this way, the NW device acts as a resistive switching model system, where electronics and ionics are decoupled and all memristive functions—nonvolatile bipolar memory, multilevel switching, selector and synaptic operations imitating Ca^{2+} dynamics of biological synapses—are exploitable.[146] Furthermore, for this kind of configuration, the electronic/ionic transport contributions in resistive switching can be easily regulated thanks to adsorbing chemical species (such as moisture) on the NW surface.[148] Thanks to the Schottky barriers of different height between the NW and the electrodes, such devices can exhibit a self-limited current that prevents Joule heating and that can be easily modeled with two back-to-back diodes and a variable series resistance.[149] Finally, short-term plasticity effects can be modeled starting from a potentiation-depression rate balance equation, where coefficients are exponentially dependent upon applied voltage, as is typical of ionic transport.[150] Formation and rupture of nanofilaments in metal-oxide NWs follow the same ECM mechanisms described in Section 3, therefore it is straightforward to expect some evidence of the quantum conductance regime. Nevertheless, while there are several examples in literature of discrete conductance levels observed mainly during the relaxation processes due to the reconfiguration of the conductive filament, such reported values are typically far from G_0 (an example is reported in Figure 11b). In 2010, Johnson et al. reported memristive properties due to electromigration phenomena in

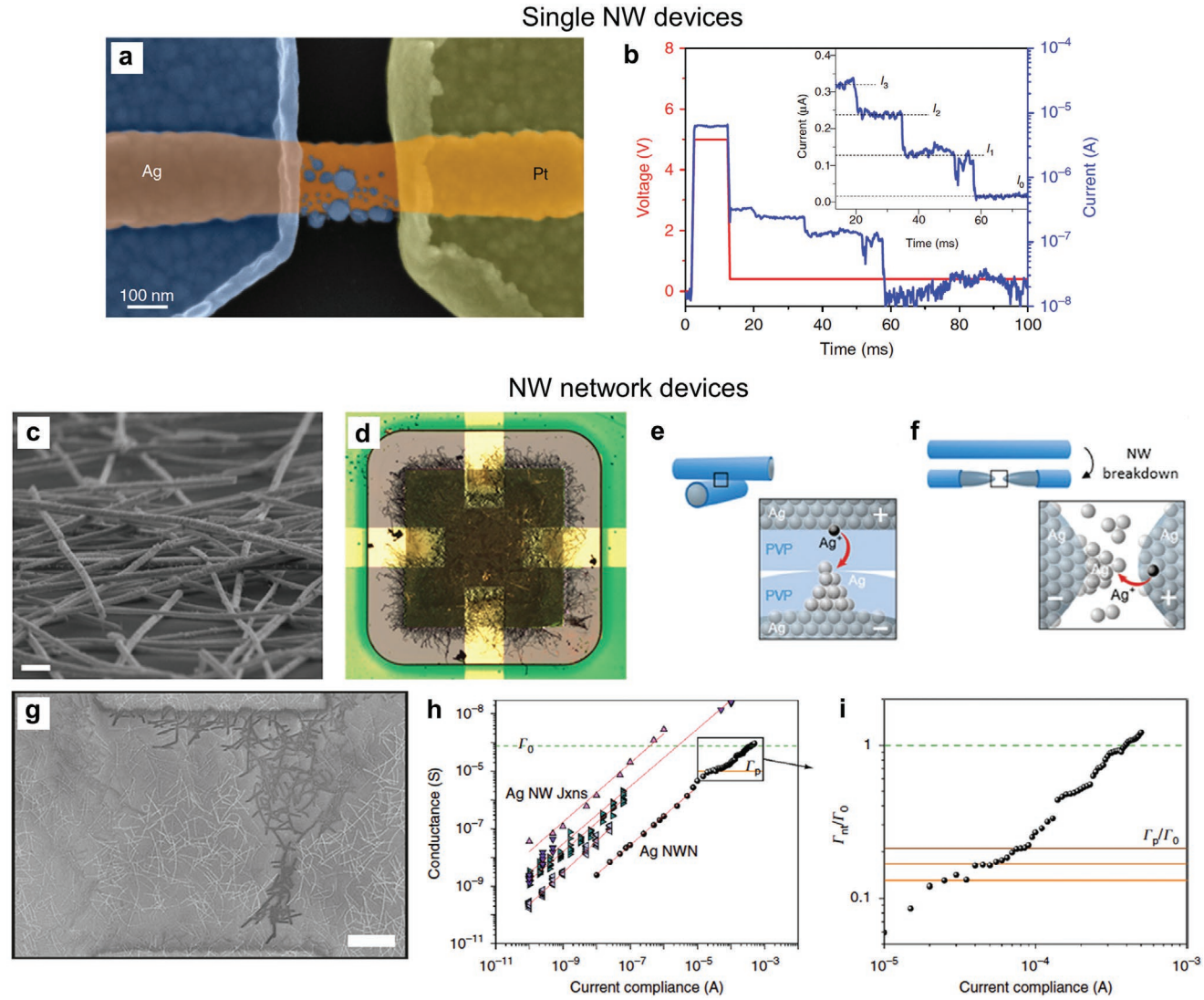

Figure 11. Quantum effects in memristive devices based on 1D materials. a) SEM image of metallic nanofilaments on NW surface, as ECM mechanism in metal oxide NWs and b) its volatile resistive switching behavior with discrete conductance values during spontaneous relaxation of the nanofilament. c) SEM image of a self-organizing NWN realized by drop-casting (scale bar: 500 nm). d) Image of a NWN self-assembled on a seed array. e,f) Sketches of memristive behavior in NW junctions (e) and in a single NW after the creation of a nanogap through breakdown (f). g) Conductive pathway in NWN highlighted by passive voltage contrast SEM image. h) Power-law dependence of conductance versus current compliance for NW junctions (Jxns) and NWN and i) zoomed view showing evidence of conductance plateaus close to quantum conductance. a,b) Reproduced under the terms of the CC-BY Creative Commons Attribution 4.0 International license (https://creativecommons.org/licenses/by/4.0).[146] Copyright 2018, The Authors, published by Springer Nature. c,e,f) Adapted under the terms of the CC-BY Creative Commons Attribution 4.0 International license (https://creativecommons.org/licenses/by/4.0).[156] Copyright 2020, The Authors, published by Wiley-VCH. d) Reproduced with permission.[158] Copyright 2012, Wiley-VCH. g–i) Reproduced under the terms of the CC-BY Creative Commons Attribution 4.0 International license (https://creativecommons.org/licenses/by/4.0).[155] Copyright 2018, The Authors, published by Springer Nature.

single-component gold NWs fabricated by top-down electron beam lithography.[151] Asymmetrical geometrical changes are induced in the initially regular Au NW due to temperature gradients caused by the applied voltage. The device switches from HRS to LRS and the minimum diameter is calculated as 35 nm^2, assuming a quantum of conductance G_0 for each atomic channel and a diameter for gold atoms of ≈0.3 nm. However, also in this case the measured conductance is not close to G_0. An interesting and rather unique example of quantum memristive NW was recently reported,[152] where single-crystal Ge was used, taking advantage of its high carrier mobility and exciton Bohr radius (24.3 nm). The NW thickness was 18 nm, so that a maximum of four current transport channels were available due to the quantum confinement. The conductivity was still dominated by charge carrier scattering because the NW length (2 mm) significantly exceeded the electron scattering mean free path in Ge, but the added sub-bands could be used to show a memristive behavior in an electrostatically modulated back-gated field-effect transistor. The Ge NW was grown by liquid injection chemical vapor deposition and included a

thin amorphous native Ge oxide shell. Thus, controlling the trap population via electrostatic gating, different configurations regarding conduction-band profiles and trap populations were achieved, resulting in a memristive *I–V* characteristics. The main limitation of this approach is the required cryogenic temperature of 78 K: at room temperature surface traps were effectively filled and the memristive behavior disappeared. Also, quantum conductance effects have been reported in resistive switching cells based on arrays of vertically aligned nanotube arrays[153] and nanorod-based composites.[154] In this scenario, it should be pointed out that a systematic study on quantum conductance effects in memristive NWs is currently missing.

A radically different approach is represented by the bottom-up realization of devices based on NW networks (also known as atomic-switch networks) that can exhibit memristive and quantum conductance effects. An NW network (NWN) is composed of bottom-up synthesized NWs that are drop-cast on an insulating substrate and then contacted with microelectrodes (Figure 11c)[155–157] or directly self-assembled on a seed array (Figure 11d).[158,159] Each NW has a metallic core (typically Ag, Cu or Ni) and an insulating shell (PVP polymer, metal oxide, or metal sulfide/iodide). The two main memristive mechanisms based on the ECM effect are schematized in Figure 11e,f. In the first case (Figure 11e), similarly to a vertical ECM cell, metal ions are moving in the NW junction from one NW metallic core to the other, forming nanofilaments in the insulating NW shells. In the second (Figure 11f), similar to a planar ECM cell and to NWs in ref. [151], a breakdown is created in the single NW due to Joule heating and electromigration effects, and metal ions are electromigrating in the so-formed nanogap. In these self-organizing systems, the nonlinear memristive dynamics is coupled to a recurrent network topology, giving rise to an emergent nonlocal behavior that resembles the way information is processed in human brain.[155–158,160] Such unique features were recently proved to be effective for "in materia" implementation of brain-inspired unconventional computing paradigms—such as reservoir computing—that can solve important tasks such as speech and image recognition with reduced training parameters.[159,161] Since the pioneering work of Stieg et al.,[158] it was shown that NWNs are characterized by collective interactions among many individual memristive elements, which in turn generate an emergent behavior that arises from complexity. The emergent behavior of the network is related to the formation of conductive pathways spanning the network connecting the stimulated electrodes, as directly visualized by lock-in thermography[162] or by SEM imaging[155] (Figure 11g). By interrogating the whole network with macroscopic electrodes, NWNs can show typical features of volatile memristive devices: a pinched hysteretic *I–V* curve, potentiation/depression of conductance, paired pulse facilitation (PPF).[156] Furthermore, the current response to appropriate voltage pulses can show metastable discrete states, with residence times ranging from milliseconds to several seconds. Such fluctuations in the global NWN conductance are due to the concurrent formation and relaxation of several local metallic nanofilaments that continuously redistribute electrical potential and current. The emerging critical dynamics in the network are typically suggested by $1/f$ power-law scaling over several temporal orders of magnitude.[158] More recently, avalanches and edge-of-chaos criticality in NWN were demonstrated and found to possibly optimize information processing for complex learning tasks.[157] How the memristive behavior of single NW junctions participates in forming an emergent network state that is characterized by a macroscopic conductance pathway is discussed by Manning et al.[155] First, they showed how the same power law $\Gamma = AI_c^{\alpha}$ can be used to fit the dependence of measured conductance versus current compliance for single NW junctions, as well as for whole NWNs (and even for planar ECM cells). This suggests that the formation of current pathways across the macroscopic network may follow the same dynamics of the nanofilaments growth across a nanoscale junction. Furthermore, the NWNs exhibited a break from such a power-law trend, with the appearance of plateaus when conductance is approaching G_0 (Γ_0 in Figure 11h,i). Starting from experimental data of single junctions, the authors simulated the network conductance in a multimodal representation, showing that the deviation from the power law appears when all the junctions involved in the macroscopic pathway are in their LRS. Such a "winner takes all" (WTA) conductance plateau is found to be G_0 divided the number n of involved NW junctions. As the current compliance is increased, additional conductance plateaus are observed, due to the creation of new paths. Very promisingly, such WTA plateaus in NWNs are claimed to be much more stable than quantum conductance levels in single NW junctions, since they represent the lowest possible energy connectivity pathway in the network.[155] In the framework of self-organizing systems, it is important to remark that quantum conductance phenomena were observed also in complex atomic-switch networks self-assembled from percolating metal nanoparticles, where the switching mechanism was reported to be related to field-induced atomic-wire formation within tunnel-gaps in between nanoparticles.[163,164]

5.4.2. 2D materials

Since the isolation of graphene in 2004,[165] research in 2D materials has been exponentially increasing, positioning them at the forefront of emergent nanomaterials. They exhibit intriguing and exotic phenomena, including quantum confinement effects,[27,166] and have great potential for a wide range of technological applications. Amongst the different functionalities of the broad family of 2D materials, resistive switching has been reported in two terminal devices based on graphene,[167] graphene oxide,[168] transition metal dichalcogenides (TMDs),[169–173] hexagonal boron nitride (h-BN),[174,175] black phosphorous (BP),[176] and some transition metal oxides.[177] Resistive switching effects have been reported in 2D materials in both a vertical configuration, where the 2D material is sandwiched in between two electrodes, and a planar configuration where lateral electrodes on the 2D material are realized (**Figure 12**a,b, respectively).

Resistive switching in 2D memristors has been explained by microscopic mechanisms such as defect/vacancy migration, filament formation, or even structural phase transitions. Although there are some reports of devices using graphene as the switching material, the most relevant use of graphene in memristive devices is as electrodes[178,179] or as a permeable layer to control ion diffusion from the metallic electrodes.[55]

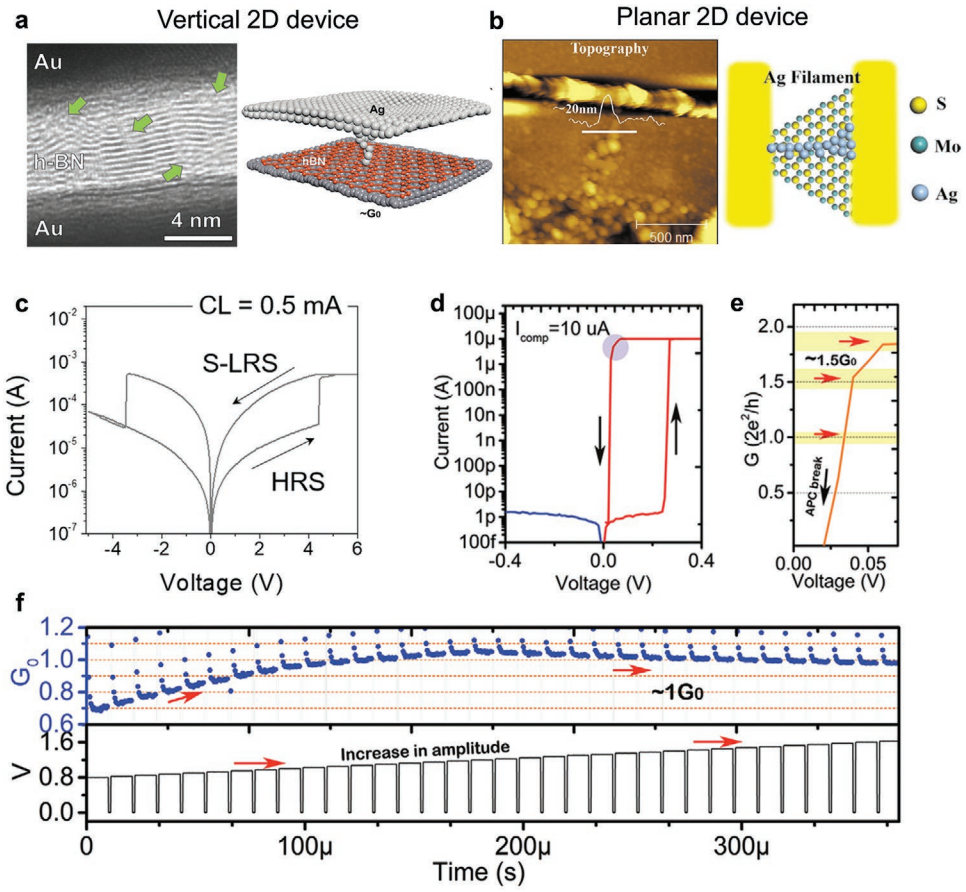

Figure 12. Quantum effects in memristive devices based on 2D materials. a) Memristive device based on 2D materials in vertical configuration. The left panel shows a TEM image of the h-BN stacks used to build cross-point memristive cells. The green arrows indicate the location of defects in the stack necessary to induce the RS. The right panel shows a schematization of a quantum point contact formed in h-BN memristive cell. Left: Reproduced with permission.[174] Copyright 2019, American Chemical Society. Right: Reproduced with permission.[175] Copyright 2021, Wiley-VCH. b) AFM topography of Ag filament in CVD-grown MoS_2 planar device with Ag and TiW electrodes. The height profile taken across the white solid line is shown. Right: Schematic volatile-switching mechanism via Ag cations diffusion into MoS2 with the consequent formation of Ag filament. Reproduced with permission.[173] Copyright 2020, Wiley-VCH. c) *I–V* curves showing resistive switching behavior in a 5 µm × 5 µm graphene-hBN-graphene device. Reproduced with permission.[174] Copyright 2019, American Chemical Society. d) Typical switching characteristic of h-BN switch device with cc = 10 µA and e) corresponding zoom of *G–V* characteristic showing the rupture of the quantum point contact. f) Modulation of quantum conductance by AC voltage pulse with fixed duration and increasing amplitude in a h-BN-based device. d–f) Reproduced with permission.[175] Copyright 2021, Wiley-VCH.

On the other hand, TMDs and in particular MoS_2 as switching layers seem to be very versatile for realizing large resistance ratios, multilevel resistance states, low power consumption switches, and even flexible devices. The realization of a non-volatile resistive switching device in a single atomic TMD layer sandwiched between electrodes has proven that these materials do have the potential to achieve the ultimate scaling level for memristive devices.[169] Stable bipolar switching with a few hundred mV threshold voltage has been achieved by using a double MoS_2 layer between Cu and Au electrodes[171] demonstrating the capabilities for low energy consumption applications (which is a critical parameter for neuromorphic computing). In the latter case, atomic-scale Cu filaments are formed while in the first example, localized and/or extended defects are responsible for the observed switching. One advantage of 2D memristors is the possibility to fabricate lateral devices in a relatively easy way.[170,173] The formation and rupture of a filament from an active Ag electrode in a MoS_2 planar device have been proposed as a promising route for engineering 2D artificial neurons.[173] Another feature of 2D memristors is the possibility to realize multiterminal devices such as MoS_2 memtransistors showing gate tunability with large resistance ratios, high cycling endurance, and long-term retention.[170] The reported electrostatic force microscopy and charge transport results were explained by the dynamic tuning of Schottky barriers at the source and drain contacts due to the doping caused by the migration of defects at grain boundaries.

Although the potential of 2D memristive devices in terms of low power consumption, high speed, and aggressive device shrinking has been recognized,[167,180,181] there is limited literature on quantum conductance effects in these systems. For example, quantum conductance steps have been observed in graphene break junctions. In this type of lateral device, the resistance switching between ON and OFF states occurs by the formation and breaking of atomic carbon chains bridging the junction.[182] The authors argue that the absence of a gate

voltage effect, the steps in conductance of G_0 and the observed voltage and temperature waiting time distributions support their conclusion that the conductance changes are due to atomic motion rather than electron or ion movement. In order to circumvent the limitations due to the modest ON/OFF ratios that can be achieved, a memory cell called rank coding is proposed. With this approach, the memory bits are stored by the conductance comparison between 2 or more devices in a single cell. The stability of the stored information is demonstrated to last for at least 24 h. Although the fabrication of the graphene junction does not involve a complicated lithographic process, it relies on the use of electrical breakdown of graphene likely compromising its reproducibility and precise control of device switching characteristics.

Resistive switching was explored also in graphene/hexagonal-boron nitride/graphene (G/h-BN/G) van der Waals sandwich structures realized through scalable methods, where the resistive switching characteristics related to the formation of atomic-sized filaments within the 2D material system was well interpreted by a model based on the nonlinear Landauer approach.[183] In a later work related to h-BN-based memristors, an intermediate state between the low resistance and high resistance states (LRS and HRS respectively) was stabilized by the use of relatively small devices and by intercalating graphene between the h-BN and metallic electrodes.[174] This intermediate soft-LRS (S-LRS) is characterized by a conductance similar to the quantum conductance G_0 and therefore likely due to the formation of atomic-size conductive filaments. This state is controlled by the use of a current compliance of 0.5 mA or 1 mA (Figure 12c) instead of the 5 mA necessary to reach the LRS. The stability of the intermediate resistance state is within one order of magnitude for a total of 300 cycles. The authors showed that the *I–V* characteristic in the S-LRS can be modeled by a hybrid system consisting of an ohmic resistance of partially formed filaments plus a quantum point conductance along with the interface between the filament and electrode. The main conclusions of this work are that the use of small devices avoids the formation of filaments at grain boundaries and the presence of graphene is crucial to reduce the metal penetration into the h-BN stack. These two factors guarantee the control of the filament size and therefore the stabilization of the S-LRS. This represents a useful guide for the design of memristive devices based on 2D materials showing stable quantum conductance states.

Nikam and co-workers[175] have recently reported quantum conductance atomic threshold switches based on an atomically thin h-BN layer sandwiched between Pt (bottom) and Ag (top) electrodes. The authors associate kinks in the device conductance G around different values of G_0 with different stages of single-atom point contact (APC) formation. Each stage ($G \ll G_0$, $G \approx G_0$, and $G \gg G_0$) can be accessed by the selection of an appropriate current compliance (Figure 12d,e). X-ray photoelectron spectroscopy indicates the presence of atomic defects that can be responsible for the switching response. From theoretical studies, it is known that h-BN can host boron or nitrogen atomic defects and these in turn can work as active sites for atomic doping and therefore change the electron conductance of the layer. In the case of the devices studied in ref. [175], the doping originates from Ag ions from the top electrodes. Endurance tests show almost no degradation of ON/OFF ratios up to 10^8 cycles and switching speed of 50 ns. Besides, the h-BN threshold switch shows good temperature stability up to 200 C and good switching uniformity in terms of the switching voltage in cycle-to-cycle and device-to-device tests. Incremental voltage pulses up to 1.5 V were used to achieve a conductance change from $0.5G_0$ to $1G_0$ (Figure 12f). The conductance remained stable when further increasing the voltage pulse up to 1.6 V, indicating that only one atomic point contact is formed within the tested area.

6. Experimental Investigation of Nanoconstrictions

To support the development of technological applications for resistive switching and quantum conduction, a large community of material scientists and solid-state physicists has moved side-by-side in the effort to enable accurate physical characterization of these phenomena. In this effort, the community has witnessed the flourishing of old and new methodologies for the direct probing and imaging of the active region responsible for resistive switching. In this framework, the development of hybrid metrology approaches that combine different metrology tools and different characterization technologies are crucial to meet the challenge of filament characterization at the nanoscale. Indeed, it has been realized that complementary methods are required to allow a quantitative analysis of the main parameters involved in the physics of QPC nanoconstrictions. For this purpose, various nanoconstriction properties must be investigated to gain insight into the QPCs physical switching mechanisms down to the single-atom level.

It has been discussed how the composition and the chemical reactions involved in the formation of nanoconstrictions allow the classification of two main types of conductive filaments. Conductive filaments induced by (a.) redox reaction creating filaments constituted by oxygen ion defects, i.e., vacancies, often referred to as anion devices, and (b.) filaments formed by the electrochemical precipitation of mobile cations migrating through the solid electrolyte layer from one active electrode, i.e., Ag or Cu, often termed cation devices. Both classes of devices present a filamentary QPC constriction, as detailed in Section 3.1 and schematically shown in Figure 4. Despite the different nature of nanoconstrictions in cation- and anion-based QPCs, some of the main parameters to be investigated can be considered as common. **Figure 13** shows a shortlist of the key parameters, including the morphology, shape/size, and volume of the active area, local conductivity, elemental composition, and chemical environment of the atoms involved. Finally, as the formation and rupture of the constriction are dynamic processes, is often ideal to study transport processes during cycling with high temporal resolution. For each type of filament, dedicated design of experiments have been reported with countless observations by means of operando, static, and in situ experiments using a wide range of techniques.[184] Scanning electron microscopy (SEM), transmission electron microscopy (TEM), scanning probe microscopy (SPM), photoemission electron microscopy (PEEM), and X-rays, to name a few, can offer information on the physical structure, including shape, size, and

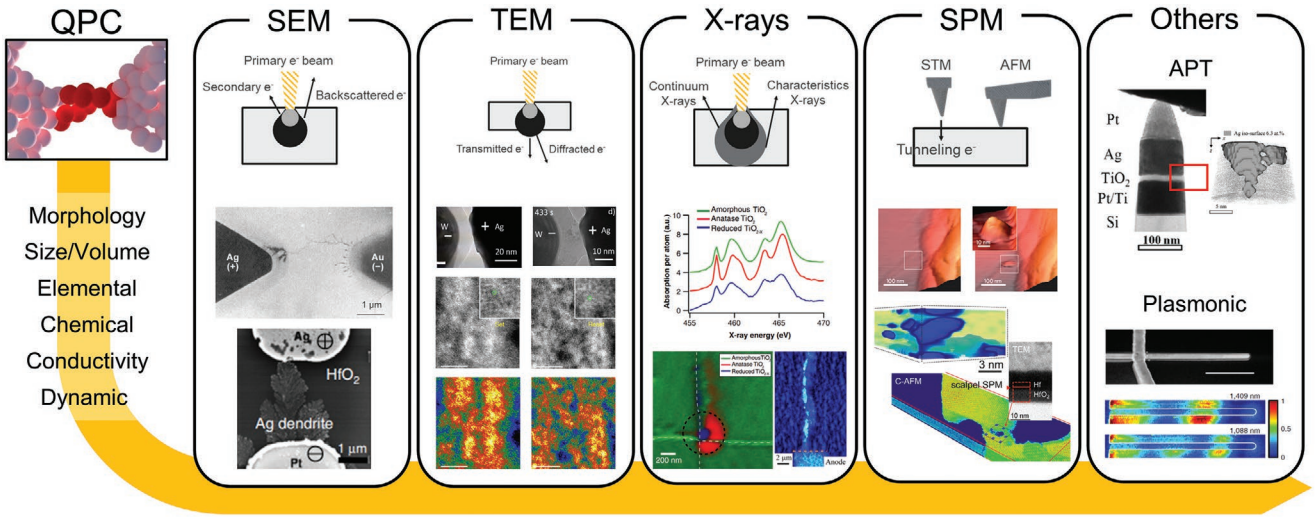

Figure 13. Overview of the physical analysis techniques available for the characterization of nanoconstrictions. The parameters to qualify the QPC are listed on the left side of the image. The most-used characterization methods include scanning and transmission electron microscopy (SEM, TEM), X-ray spectroscopy, and scanning probe techniques, these have been used in various operando, static, and in situ experiments to generate a wealth of knowledge on nanoconstrictions. In parallel, the readouts from established techniques have been correlated with emerging methodologies such as undirect probing schemes based on nanoplasmonics, atom probe tomography, and tomographic sensing with scalpel SPM. All combined, this enabled a complete view of the main parameters describing the physical properties of the nanoconstrictions and their operations for resistive switching application. Panels in the "SEM" section: Middle: Adapted with permission.[190] Copyright 1976, AIP Publishing; Bottom: Adapted with permission.[213] Copyright 2007, AIP Publishing. Panels in the "TEM" section: Second row: Reproduced with permission.[45] Copyright 2013, Springer Nature; Bottom two rows: Reproduced with permission.[203] Copyright 2014, Springer Nature. Panels in the "X-rays" section: Bottom right: Reproduced with permission.[202] Copyright 2009, AIP Publishing; Middle and bottom left: Reproduced with permission.[214] Copyright 2011, IOP Publishing. Panels in the "SPM" section: Two images on middle row: Reproduced with permission.[187] Copyright 2012, Springer Nature. Panels in the "Others" section: Image for "ATP": Reproduced with permission.[212] Copyright 2017, Wiley-VCH; images for "Plasmonic": Reproduced with permission.[215] Copyright 2015, Springer Nature.

atomic arrangement of the QPC, and when the nanoconstriction dimensions allow, chemical information can be revealed via energy-dispersive X-ray spectroscopy (EDS) and hard X-ray photoelectron spectroscopy (HAXPES). However, when probing changes to the filament electronic structure, the list of available techniques reduces dramatically and SPM has proven very valuable, as reported in multiple works using STM, Kelvin probe force microscopy (KPFM), pressure modulated conductance microscopy (PMCM), and conductive atomic force microscopy (C-AFM), among others.[185–189]

SEM was one of the first analytical methods to detect the presence of conductive filaments. From the classic paper by Hirose and Hirose where the dendritic morphology of a micro-sized Ag filament is made visible on the surface of an As_2S_3 thin film, to the most recent (top-view) observation of nano-sized filaments in ultrascaled dot cells.[190–192] Considering the resolution limit of modern equipment, SEM remains a valid option for in/ex situ analysis of filaments with dimensions in the range of 10–100 nm, provided that the material constituting the active region offers sufficient imaging contrast via compositional differences compared to the surrounding area. Although the use of SEM for direct observation of ultrascaled QPCs is partially limited, it should be emphasized that electron-beam-induced current (EBIC) and electron beam-absorption current (EBAC) imaging methods inside the SEM have been shown to be very efficient methods for filament localization in vertically integrated devices where the top electrode is accessible to the electron beam.[193] As an example, Hayakawa et al. used SEM as a fast methodology to study filament position in a large set of devices and allowed them to demonstrate filament position control in scaled capacitors by tuning the thickness of the switching layer.[191]

To characterize the presence and the elemental composition of the filament, TEM remains among the most informative techniques and has been widely used for sensing dynamic events during programming (QPC growth) and erasing (QPC rupture or modulation).[45,194] The recent introduction of TEM sample holders that allow for electrical biasing and heating of the sample while sensing, has provided a rapid boost to the field of in situ and operando analysis of dynamic phenomena, where standard cross-sectional sample preparation has been complemented with the analysis of in-plane structures for filament observation.[195–197] Here, it is important to mention that fast ion migration processes under high electric field (ca. sub-nanosecond) pose certain limitation to TEM data collection in observing the switching processes due to finite spatiotemporal resolution. Of particular note, beyond the characteristic shape and size of the filament, TEM enables a clarification of the role of cation mobility and redox reaction rates in filament growth modes.[198,199] Interesting new results are emerging from the development of techniques based upon the emission of secondary electrons (SEEBIC) and integrated differential phase contrast (iDPC) modes in TEM that are sensitive to local electric fields with nanoscale resolution.[200]

For the analysis of microscale redox processes occurring inside the switching layer, X-ray techniques including PEEM and HAXPES have been able to provide valence states of the filament in different conductive states.[201,202] High spatial

resolution of electron energy loss spectroscopy (EELS) and Auger electron spectroscopy (AES) depth profiles performed before and after switching events in the area of the filament, contributed to the demonstration of the sub-stoichiometric nature of the conductive channels in Ta_2O_5-based devices formed due to the migration of oxygen vacancies.[195,198,203] These works have been instrumental in the understanding of the role of charged migrating oxygen ions in the switching events.

In the SPM field, STM and atomic force microscopy (AFM) have contributed to the analysis of materials used for resistive switching. The localized tip-induced electrical switching of the sample surface has been used to explore the geometrical and electrical properties of conductive filaments in a large set of materials including NiO_x, TiO_2, and HfO_2 to name but a few. Here, STM has been vital in enabling us to induce and visualize the electrochemical formation and dissolution of atomic clusters.[54,204] On the other hand, AFM with all its secondary electrical imaging modes, can be used to correlate the morphological changes in the nanoconstrictions with multiple electrical parameters, such as resistance, capacitance, and work function. This availability of signal readouts, combined with a remarkable filament localization capability, comparable to that of TEM and EBIC, has converted SPM methods in some of the most used analytical techniques for failure analysis and reliability studies, involving the use of the nanosized tip as an active electrode for filament formation, or purely as a passive probe.[188,205,206] An interesting novel solution was offered by the concept of tomographic sensing with AFM, often referred to as tomographic-AFM (TAFM) or scalpel SPM.[207–209] Here, tip-induced nanoscale abrasive wear in contact-mode AFM, is used for the sub-nanometer material removal obtaining a controlled milling of the surface in combination with the acquisition of the secondary AFM readout (i.e., electrical information). Through the acquisition of 2D profiles obtained for different depths of the sample, this approach enables tomographic sensing capabilities for techniques that were previously limited only to surface sensitivity. To date, this approach has been demonstrated on various materials, e.g., metals, dielectrics, and semiconductors, reaching controlled removal rates in the range of a fraction of a nm per scan. Applications have been found for the 3D reconstruction of buried features in bulk thin films, sensing properties such as conductivity, photogenerated carriers, and piezoelectric coefficient. For the observation of conductive filaments, scalpel SPM has been used with conductive atomic force microscopy (C-AFM), obtaining a resolution of around 3 nm for electrical features in voxel size in the order of 1000 nm^3.[210] Clearly, the technique is destructive as the area of interested is completely removed at the end of the analysis. In addition, by directly accessing the conductive filament active region, the tip–sample interaction must be controlled to minimize any modification of the filament during the analysis, this includes the tip–sample load force, tip material, and scanning environment. A clear example is represented by the spontaneous oxidation filaments constituted by oxygen vacancies if the measurement is performed in an air environment. A powerful alternative for 3D compositional and structural analysis with atomic resolution is offered by atom probe tomography (APT).[211] Here, the sample is a needle-shaped specimen with a hemispherical tip of less than 100 nm in diameter that is prepared by a process flow similar to that used for TEM lamella preparation. During the analysis, controlled laser-assisted field-ionization and -evaporation of surface atoms from the specimen are induced, and the evaporated ions are accelerated by the applied electric field toward a position-sensitive detector. Once on the detector, the ion's time-of-flight provides combined spatial and chemical information while the 3D information, i.e., the original (x,y,z) position of atoms, is derived from the controlled, sequential evaporation of the atoms and reconstructed by a stereographic projection model. To date, the APT method has been successfully applied to $Ag/TiO_2/Pt$ devices, demonstrating how crystalline Ag-doped TiO_2 forms at vacant sites on the device surface acting as the conductive filament in these devices.[212] In addition, the authors studied the role of current compliance on the resulting filaments, obtaining direct evidence of the transition between nonvolatile and threshold-switching electrical characteristics as a function of filament morphology.

In this section, we showcased some of the significant progress made in the recent years in the physical characterization and metrology of nanoconstrictions. This collection of impressive results also demonstrates the considerable challenges associated with the task. The investigation of dynamic phenomena at relevant temporal resolution (in the femtosecond to nanosecond regime) remains complex. For example, ultrafast TEM and (fourth generation) synchrotron light sources are important tools to study transient states of filaments at the relevant scales. Similarly, accessing 3D information from ultraconfined volumes of material remains possible only with emerging and less established techniques. This is the case for APT and scalpel SPM. In APT, important challenges arise from complex sample preparation. Here, the need for positioning the area of interest in the center of the needle-shaped specimen by focused ion beam (FIB) often leads to damage of the filament due to Ga+ ion implantation, defect generation, layer amorphization, and intermixing, to name a few. In scalpel SPM, the current implementation relies on a single probe tip used for sensing as well as for the nanoscale material removal. This dual use represents conflicting tip requirements namely 1) an ultrafine tip for probing, and 2) a robust tip for material removal due to tip wear during high-pressure contact. Moreover, the use of one single tip is not compatible with the need to combine techniques that require different probes (e.g., KPFM and STM).[216] The rapid tip degradation during the removal process calls for frequent probe replacement, resulting in time-consuming and low-throughput measurements and the introduction of tip-induced artifacts and variability. Therefore, the future development of new instrumental capabilities is expected to become more important for the development of technological applications and is key to continued understanding of physical effects in nanoconstrictions.

7. Applications of QPC Memristive Devices

Application of quantum point contact memristive devices in memory and logic elements, biologically plausible synaptic and neuron devices, unconventional computing architectures, and metrology are schematized in **Figure 14** and discussed in the following.

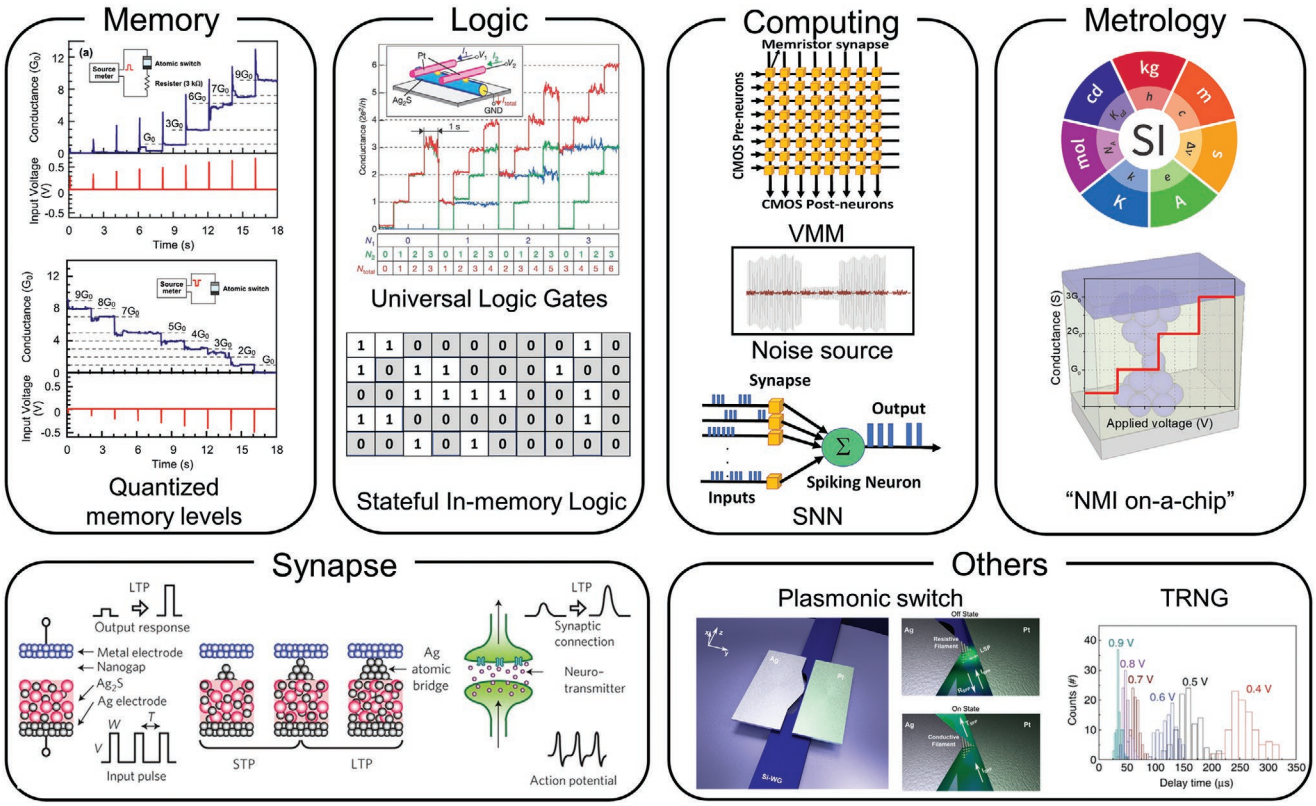

Figure 14. Application of quantum point contact memristors in memory and logic elements, in biologically plausible synaptic devices, in various unconventional computing architectures, in metrology, in ultrasensitive charge and photon detection and in hardware security applications. The multilevel memory operation, arising from distinct quantum conductance states achieved by careful control over the formation, evolution and rupture of the ballistic conductance channel, has been demonstrated by Tsuruoka et al. Images for "Memory": Adapted with permission.[105] Copyright 2012, IOP Publishing. Demonstration of AND, OR, and NOT logic gates by exploiting the bistable switching characteristics of quantum conductance in $Ag/Ag_2S/gap/Pt$ memristors and schematic representation of construction of stateful In-memory logic circuit. Images for "Logic": Top: Adapted with permission.[38] Copyright 2005, Springer Nature. Schematic representation of different unconventional computing architectures such as vector-matrix-multiplication (VMM) within a memristor crossbar array can be achieved through QPC memristors using the analog synaptic conductance behavior, spiking neural networks (SNN) using stochastically firing neuron behavior of the memristors and as tailorable noise source for nondeterministic computing architectures. Application of memristive devices for metrology, where the quantum conductance effects can be exploited for the realization of electrical standards. The SI logo is reproduced under the terms of the CC-BY Attribution 4.0 international licence (https://creativecommons.org/licenses/by/4.0). The schematization of quantum steps in memristive devices. Images for "Metrology": Top: SI logo is reproduced under the terms of the CC-BY Creative Commons Attribution 4.0 International license (https://creativecommons.org/licenses/by/4.0).[246a] Copyright Bureau International des Poids et Mesures; Bottom image: Adapted with permission.[246b] Copyright 2020, Wiley-VCH. Replication of biologically plausible synaptic plasticity mechanisms by modulation of activation pulse frequency by Ohno et al. Images for "Synapse": Adapted with permission.[227] Copyright 2011, Springer Nature. Schematic of the atomic scale plasmonic switch showing a planar silicon photonic waveguide structure with a plasmonic Ag/a-Si/Pt slot waveguide on top of it. Due to the presence or absence of QPC in the Ag/a-Si/Pt memristor, the properties of the plasmonic cavity are modified to have two distinct plasmonic resonance states. Images for "Others: Plasmonic Switch": Adapted with permission.[242] Copyright 2015, American Chemical Society (https://pubs.acs.org/doi/full/10.1021/acs.nanolett.5b04537; further permissions related to the material should be directed to ACS). Memristive devices working in the quantum regime in hardware security applications where true random number generation (TRNG) can be achieved utilizing the probabilistic switch characteristics. Image for "Others: TRNG": Adapted under the terms of the CC-BY Creative Commons Attribution 4.0 International License (https://creativecommons.org/licenses/by/4.0).[134] Copyright 2017, The Authors, published by Springer Nature.

7.1. Multilevel Data Storage

Quantum-point contacts formed in MIM memristive devices form the basis for multilevel data storage within a single memory cell. As memristive device performance depends critically on the dimension of the conducting filament, there is a possibility that the devices can be scaled down to the dimension of a single filament or even to the single-atomic level. Therefore, devices of a few nanometers in size are possible,[217] without degradation of performance. Indeed, scaled devices were found to work more reliably due to the physical confinement of the filament. Additionally, due to the simplicity of the MIM structure, 3D vertical integration in multiple layers and also in CMOS back-end processes is possible. Li et al.[218] showed vertical stacking of 5 layers of conducting filamentary memristive devices, which can enable ultrahigh-density memory integration. Additionally, high speed and low energy consumption make such structures attractive for computing-in-memory (CIM) architectures, as described later in this article. However, a reliable, low-noise and reproducible readout of intermediate conductance states require superior control over the formation, maintenance, and evolution of QPCs and

filaments in response to a series of multiple stimuli. Due to the inherently stochastic nature of the filament formation and thermal-noise-induced instability, it is highly challenging to obtain and maintain these multiple conductance states reliably in QPC memristive devices. Intensive research efforts in this direction are underway and can ensure ultrahigh-density multilevel data storage with high precision in a single cell possible. A few promising approaches, such as nanopatterning of the top Ag electrodes, were shown to result in confined filament structures, leading to a better switching uniformity.[219,220] Devices with patterned nanodot electrodes exhibited excellent bidirectional threshold switching performance, including low leakage current (<1 pA), high on/off ratio (>10^8), high endurance (>10^8 cycles)[220] where patterned nanocone arrays showed four resistance states, stable data retention, and switching uniformity.[219]

7.2. Selectors

RRAM technology critically depends on access devices to reduce the sneak path current issue in large crossbar arrays of devices. A two-terminal access device, also known as a selector, can solve the sneak current issue. Selectors must have a high current–voltage nonlinearity and low leakage current at a small bias. Different quantum-point contact switches could offer high *I–V* nonlinearity, steep, low-power turn-on slope, picoampere (pA) OFF-state leakage current, and fast switching speed and are, thus, of great interest as selectors. For Pd/Ag/HfO_x/Ag/Pd devices, for instance, an on/off ratio of 10^9 or above, off current less than pA, ON-switching slope less than 1 mV dec^{-1} and bipolar threshold switching is reported, which makes them extremely attractive as selectors.[221] Selectors could be easily integrated with a nonvolatile drift memristor for large array applications. For ferroelectric field-effect transistor (FeFET) technology, a known roadblock is the degradation of the memory window (MW) and on/off ratio when operating at low programming voltage. This voltage-MW trade-off can be bypassed using a QPC switch in series with a FeFET. This has been shown[222,223] in FeFETs with Si or oxides as channel semiconductors, where a switch can significantly open up the memory window by inducing a sudden off to on transition while the reverse transition is governed by the FeFET and therefore even within <3 V range, a sizable MW and on/off ratio from a FeFET is possible.

7.3. Logic

Terabe et al. demonstrated that all logic circuit requirements, i.e., nanoscale device size, > GHz switching speed, and sub-1 V operation voltage, can be fulfilled using QPC devices. By exploiting the bistable switching characteristics of quantum conductance in Ag/Ag_2S/gap/Pt memristors, construction of AND, OR, and NOT logic gates have been demonstrated.[38] These three being the universal logic gates, any subsequent logic circuits can be built based on these. An example of reconfigurable amplifier circuits has been proposed by Ibrayev et al.[224] based on quantum conductance devices in combination with MOSFETs. A discretized control of resistor values in the amplifier circuits is possible using these quantum conductance memristive devices. As resistors play a major role in the biasing and control of MOSFET amplifier parameters, the replacement of resistors with memristive devices offers several advantages in comparison to a resistor-based design, in terms of power dissipation, on-chip area, and total harmonic distortion values. Utilization of quantum electrical resistance of the memristive devices to represent logic information can also be useful for simultaneous implementation of Boolean logic and latch functions. Although several stateful logic operations have been reported using memristive systems, advancement of the stateful logic technology depends critically on the improvement of switching uniformity. With improved device uniformity, increased energy and time efficiency can be achieved. Kim et al.[225] showed that with improved device uniformity, the total number of steps for n-bit full adder execution can be reduced to 2 ns. Issues arising from unwanted switching of memristive devices after prolonged bias stress or the nonlinear switching dynamics of the memristors can also be resolved with a periodic refresh step that can eliminate the lurking error factor. Also minimizing the parasitic resistance component can improve the success rate of the gate operation. A thorough review on this topic is recommended for the interested readers.[226]

7.4. Synaptic Plasticity

While precision computing is one significant goal, mimicking biological neuroplasticity is another target for AI-on-chip and edge-computing hardware. Depending on the amplitude, duration and frequency of input voltage pulses, modification of the ionic filament strengths can be regulated significantly in quantum memrsitive devices to replicate the biological action potential and synaptic connection, leading to two basic types of synaptic plasticity, i.e., short-term plasticity (STP) and long-term potentiation (LTP).[227] Also paired-pulse facilitation (PPF) and paired-pulse depression (PPD) has been demonstrated in quantum memristive devices.[228] By precisely modulating the stimulation rate, control over the synaptic plasticity can thus be obtained, which can lead to effective synaptic learning operations.

7.5. Synaptic Weight Element

The quantum conductance phenomena, occurring in metal oxide memristive devices, also have great potential for analog synaptic weight update for effective training of artificial neural networks (ANNs). Continuous, linear, and symmetrical modulation of the device conductance, in response to identical programming pulses, is an issue of vital importance for blind synaptic weight updates during training in ANNs. In a recent study, a scanning probe microscope (SPM) assisted electrode engineering strategy was shown to control the ion migration process to construct single conductive filaments in Pt/HfO_x/Pt devices.[229] Sensitive tuning and evolution of the filament in these devices, achieved through the deliberate design of the electrode/switching matrix interface with the SPM tip, led to 32 half-integer quantum conductance states in the range of

$0.5G_0$ to $16G_0$ with enhanced distribution uniformity. Simulation results revealed that the numbers of the available quantum states and fluctuation of the individual conductance states play an important role in determining the overall performance of the neural networks. The 32-state quantum conductance behavior of the hafnium oxide devices resulted in improved recognition accuracy, approaching 90% for handwritten digits, based on analog-type operation of the multilayer perception neural network. In another approach, a Si memristor with alloyed conduction channels showed a stable and controllable device operation, which enables the large-scale implementation of crossbar arrays. The conduction channel, formed by silver (Ag) as a primary mobile metal alloyed with silicidable copper (Cu) stabilized the switching. For an optimal alloying ratio, Cu is found to effectively regulate the Ag ion movement, contributing to a substantial improvement in the spatiotemporal switching uniformity, a stable data retention over a large conductance range, and a substantially enhanced programming symmetry in analog conductance states. With these memristive devices, a large-scale crossbar array is demonstrated that leads to a high device yield and accurate analog programming capability.[230]

7.6. LIF Neurons

Another possible application area for the memristive devices operating in the quantum regime is the demonstration of stochastically firing leaky integrate-and-fire (LIF) neurons. These electronic neuron devices, based on a discrete scalable diffusive memristor, work on the principle of accumulation of subthreshold input pulses and firing once a threshold is reached. The randomness of the Ag or Cu ion dynamics under electric field mimics the actual neuron ion channels. Neuronal firing frequency and recovery periods can be modified either by engineering the device stack and geometry or at the circuit level, e.g., by using additional RC circuits. Single-cell LIF neurons can drastically reduce the active area needed for neurons in contrast to traditional CMOS-based approaches that require tens to hundreds of transistors, improving the possibility of scaling up the number of neurons in the circuit, and improving the system performance. Utilizing the LIF functions, single memristive neurons have been shown to perform unsupervised synaptic weight updating and pattern classification on integrated memristive convolutional neural networks.[231]

7.7. Alternative Computing Approaches

In another significant finding, Yi et al.[125] showed that the randomness and severe electronic noise in the devices near the atomic point-contact regime, which would be a challenge for nonvolatile memory applications[232] can actually be beneficial in some applications. One example of such application is signal processing via stochastic resonance phenomena, where the addition of white or $1/f$ noise can improve the response of a nonlinear system to subthreshold signals.[233–235] This phenomenon suggests an important role for noise in information processing. In the biological brain, stochasticity in synaptic inputs can help in cognitive processes such as decision making and learning.[236,237] In TaO_x memristors, disruption of electronic eigenstates by atomic thermal fluctuations in a point contact can result in inherent state instability and result in efficient random data generation in cryptography and in stochastic computing.[125]

7.8. Tailorable Noise Source

Fluctuation and noise near the quantum point contact regime can also act as an ideal candidate for tailorable noise sources. A possible application has been shown in the scheme in ref. [238], where a memristor crossbar array accelerates the operation of a Hopfield neural network by performing the vector-matrix multiplications in single time steps. For a targeted computational problem using a memristive tunable noise source, first a larger noise was applied to find the global minimum in the energy landscape and then the noise was gradually decreased according to the simulated annealing protocol.[140] Experimentally, it was shown that the approach can solve nondeterministic polynomial-time (NP)-hard problems by harnessing the intrinsic hardware noise. Simulations suggest that memristive approaches can offer a solution throughput over four orders of magnitude higher per power consumption relative to current quantum, optical and fully digital approaches.[239]

7.9. Hardware Security

Today's data encryption systems rely on deterministic processes such as pseudo random number generators (PRNGs) to generate randomness. They are vulnerable to cyber-attacks as the working principle of these systems still relies on deterministic and thus predictable algorithms. A better solution is to use hardware PRNGs. However, not all of them are equally reliable and therefore a statistically varying PRNG is of vital interest. Realization of hardware security through the generation of random numbers is possible using quantum point contact devices. For $Ag:SiO_2$ diffusive memristor, Jiang et al.[134] showed that memristive true random number generators (TRNG) can provide incomparable advantages in scalability, circuit complexity, and power consumption. Nanoparticle dynamic simulation and analytical estimates confirm that the stochasticity in delay time, due to the probabilistic process of Ag particle detachment from an Ag reservoir, results in TRNG behavior. The random bits generated by the diffusive memristor TRNG were shown to pass all 15 NIST randomness tests. This operating principle can pave the way for memristive-based hardware security applications for the edge devices in the IoT era.

7.10. Atomic-Switch-Based Systems

Atomic switches show unique advantages in many applications other than nonvolatility, low-power consumption, and high on/off ratios. Extreme scalability has given impetus to this technology toward commercialization. The development of various atomic switches, i.e., two-terminal and three-terminal, volatile, and nonvolatile, has made atomic-switch

technology universal.[240] Atomic-switch field-programmable gate array (FPGA) technology has been shown to have promising applications in IoT sensing systems in space.[241] As electronics working in space have demanding requirements, like operability in a broad temperature range, radiation tolerance, lightweight, and compact components, the atomic-switch-based logic can supply considerable advantages. For example, an infrared image sensor requires circuitry for fast and compact onboard signal processing to avoid transmission loss. For this task, a lossless image compression function is required without adding significant size, mass, and power consumption for the onboard electronics of satellites. A series of complementary atomic switches (CAS), composed of two Cu atomic switches with a polymer solid electrolyte sandwiched between two metals (Cu and Ru), is utilized in lookup tables and crossbar switches in an FPGA with good reproducibility and retention. The FPGA chip was used to perform several dedicated operations for an infrared image detector including superposition, mean, median, and normalize functions to improve intensity. A huge improvement in area and power efficiency is reported from the CAS-based FPGA chip.

7.11. Atomic Plasmonic Switch

Electrically controlled atomic-scale plasmonic switches are an interesting approach that has the potential to make photodetection possible at the single-atom scale. An experimental demonstration of atomic-scale plasmonic switch was reported by Emboras et al.[242] utilizing a planar silicon photonic waveguide structure with a plasmonic Ag/a-Si/Pt slot waveguide on top. The silicon waveguide provides the optical signal into a Ag/a-Si/Pt slot, where the optical signal is converted into a gap plasmon. The presence or absence of a quantum point contact in the Ag/a-Si/Pt memristive device alters the properties of the plasmonic cavity to allow it to have two distinct plasmonic resonance states. This reversible digital optical switching, operating at room temperature with an extinction ratio of 9.2 dB up to MHz frequencies with femtojoule (fJ) energy consumption, opens promising pathways for fast atomic photodetection. By exploiting the interplay between electrical, optical, and light-induced thermal forces, platforms for combined electronics and photonics at the atomic scale can be realized.[243]

7.12. Quantum Metrology

The revision of the International System of Units (SI) in 2019 brought with it a radical change in metrology, since units have been defined in terms of fundamental physical constants,[244,245] memristive devices can be exploited as platforms for quantum metrology.[246b] As a direct consequence of the revised SI, each experiment or device that is able to correlate a physical observable to a constant of nature (or even a combination of constants) that has been assigned to a fixed (exact) numerical value becomes a direct realization of the corresponding unit. Note that in this framework the uncertainty in the realization of units depends on the specific scientific/technical purpose. In the case of memristive quantum devices, the physical observable represented by the fundamental quantum of conductance G_0 depends only on physical constants (the electron charge e and the Plank constant h) that have been fixed in the revised SI. For this reason, these devices can be exploited for the practical realization of a quantum-based standard of resistance that, differently from conventional resistance standards based on the quantum Hall effect,[247] can work at room temperature, in air and without the application of a magnetic field. For this reason, memristive devices can be exploited for the on-chip integration of fundamental units towards the realization of self-calibrating systems with zero-chain traceability, envisioning the implementation of the "NMI-on-a-chip" concept (where "NMI" stands for "National Metrological Institute").

7.13. Readout for Quantum Computers

Design of a quantum point contact adjacent to a quantum dot has been shown to produce a high-level sensitivity to single-electron charging in the quantum dot.[248] In a mechanically formed constriction on top of a 2DEG at the interface of a GaAs/AlGaAs semiconductor heterostructure, and using a bias that allows conductance of $G_0/2$, allowed maximum sensitivity to charge detection. An increase in detection sensitivity by 73% over the conventional design is reported in these structures. Similar innovative designs can be engineered in electrochemically formed quantum point contacts also to make them suitable for extremely sensitive charge detection, in which they are able to detect single electrons, making them potential candidates for readout devices in quantum computers.

8. Conclusion and Perspectives

Although the unique properties of these two-terminal devices allow investigation and exploitation of quantum effects at room temperature, the potential of memristive quantum devices is still somewhat unexplored. Despite the great attention that has been devoted in last several years toward the understanding and engineering of the switching mechanism underlying memristive functionalities, the observation of quantum effects in memristive devices is not straightforward. In this context, detailed knowledge of resistive switching behavior at the near-atomic scale and a rational design of memristive devices working in the quantum regime is still missing.

The origin of stepwise variations in memristive conductance still needs further investigation to understand the relationship between this phenomenon and the discrete atomic structures of the conductive filaments. In this context, shot noise analysis, magnetic-field-dependent measurements, and superconducting subgap spectroscopy can shed new light on the atomic-sized nature of metallic filaments. In order to control and dominate quantum conductance levels, the relationship between materials/interfaces involved and corresponding device functionalities still have to be disclosed. Also, operating conditions and parameters such as voltage and/or current stimulation modes have to be properly investigated in conjunction with materials/device engineering to obtain stable and reproducible quantum levels. Potential approaches for reliable control of QPCs in

memristive devices involve: i) nanostructuring of the electrodes to improve the localization and reproducibility of the nanofilament formation; ii) identification of the proper working operation conditions (stimulation/support voltage and/or current); iii) controlling device dynamics through temperature-controlled measurements; iv) proper selection of materials to regulate the driving forces that cause the filament dissolution; and v) monolithically integrated memristive elements with readout electronics that minimize the effects of interconnect instability, parasitic, and noise effects. In ECM cells, this includes the selection of materials by considering the Gibbs energy of filament formation in relation to the surrounding matrix. In VCM cells, this includes the selection of materials with more positive standard redox potential to increase the filament stability. All these strategies require a deep understanding of the interplay in between supportive and destructive forces at the nanoscale acting on the nanosized filament. In this scenario, it is worth mentioning that the ability of operating memristive devices in the quantum regime can potentially represent a significant advantage for reducing power consumption since only a few atoms are needed to be electrically moved to overcome the energy barriers between two switching configurations.

The atomic size of the nanofilament constriction brings new challenges for nanoscale characterization, necessary for obtaining new insights into the fundamental physics underpinning this technology. High throughput nanometrology and advances in nanoelectrical characterization techniques are required to investigate not only the nanoconstrictions with nearly atomic resolution but also their surroundings for a deep understanding of the interaction between the nanofilament and its matrix. This aspect is also fundamental for obtaining stable and reproducible quantum levels. In this scenario, one of the main challenges is represented by the development of an "hybrid metrology" approach at the nanoscale that takes into advantage of the strengths of two (or more) metrology techniques for providing a more meaningful measurement of the same measurand than these techniques can individually provide.

From a theoretical perspective, efforts are still required for a deep understating of the origin of noninteger and sub-G_0 quantum levels. The effect of nonideal factors including scattering, electron correlation effects, and filament geometry and microstructure on the theoretical Landauer approach used to describe quantum phenomena in memristive devices needs further investigation. Furthermore, behavioral models which take quantum effects into account have to be developed to allow us to analyze the implementation of memristive quantum devices in circuits and computing architectures. From the technological point of view, wafer-scale uniformity of switching materials is of vital importance for scaling up QPC-based circuit complexity with desired performance levels.

All the abovementioned aspects represent key requirements for understanding and controlling quantum effects for the implementation of memristive devices as versatile quantum platforms for investigating physical phenomena such as magnetic, superconductive, and thermoelectric behavior of nanoconstrictions and nanocontacts, and the development of new device concepts and quantum systems based on quantum physical phenomena arising at the nanoscale.

Acknowledgements

This work was supported by the European project MEMQuD, code 20FUN06. This project (EMPIR 20FUN06 MEMQuD) has received funding from the EMPIR programme cofinanced by the Participating States and from the European Union's Horizon 2020 research and innovation programme.

Open Access Funding provided by Istituto Nazionale di Ricerca Metrologica within the CRUI-CARE Agreement.

Conflict of Interest

The authors declare no conflict of interest.

Keywords

ballistic transport, memristive devices, quantized conductance, quantum conductance, resistive switching

Received: February 7, 2022
Revised: March 23, 2022
Published online: July 1, 2022

[1] G. E. Moore, *IEEE Solid-State Circuits Soc. Newsl.* **2006**, *11*, 33.
[2] R. Dennard, F. Gaensslen, W.-N. Yu, L. Rideout, E. Bassous, A. L.e Blanc, *IEEE J. Solid State Circuits* **1974**, *9*, 256.
[3] R. S. Williams, *Comput. Sci. Eng.* **2017**, *19*, 7.
[4] M. M. Waldrop, *Nature* **2016**, *530*, 144.
[5] M. A. Zidan, J. P. Strachan, W. D. Lu, *Nat. Electron.* **2018**, *1*, 22.
[6] D. V. Christensen, R. Dittmann, B. Linares-Barranco, A. Sebastian, M. L. Gallo, A. Redaelli, S. Slesazeck, T. Mikolajick, S. Spiga, S. Menzel, I. Valov, G. Milano, C. Ricciardi, S.-J. Liang, F. Miao, M. Lanza, T. J. Quill, S. T. Keene, A. Salleo, J. Grollier, D. Markovic, A. Mizrahi, P. Yao, J. J. Yang, G. Indiveri, J. P. Strachan, S. Datta, E. Vianello, A. Valentian, J. Feldmann, et al., *Neuromorphic Comput. Eng.* **2022**, *2*, 022501.
[7] L. Chua, *IEEE Trans. Circuit Theory* **1971**, *18*, 507.
[8] D. B. Strukov, G. S. Snider, D. R. Stewart, R. S. Williams, *Nature* **2008**, *453*, 80.
[9] R. Waser, M. Aono, *Nat. Mater.* **2007**, *6*, 833.
[10] J. J. Yang, D. B. Strukov, D. R. Stewart, *Nat. Nanotechnol.* **2013**, *8*, 13.
[11] Z. Wang, H. Wu, G. W. Burr, C. S. Hwang, K. L. Wang, Q. Xia, J. J. Yang, *Nat. Rev. Mater.* **2020**, *5*, 173.
[12] N. K. Upadhyay, H. Jiang, Z. Wang, S. Asapu, Q. Xia, J. J. Yang, *Adv. Mater. Technol.* **2019**, *4*, 1800589.
[13] D. Ielmini, H.-S. P. Wong, *Nat. Electron.* **2018**, *1*, 333.
[14] Y. Zhang, Z. Wang, J. Zhu, Y. Yang, M. Rao, W. Song, Y. Zhuo, X. Zhang, M. Cui, L. Shen, R. Huang, J. J. Yang, *Appl. Phys. Rev.* **2020**, *7*, 011308.
[15] J. J. Yang, M. D. Pickett, X. Li, D. A. A. Ohlberg, D. R. Stewart, R. S. Williams, *Nat. Nanotechnol.* **2008**, *3*, 429.
[16] R. Waser, R. Dittmann, G. Staikov, K. Szot, *Adv. Mater.* **2009**, *21*, 2632.
[17] I. Valov, W. D. Lu, *Nanoscale* **2016**, *8*, 13828.
[18] Y. Li, S. Long, Y. Liu, C. Hu, J. Teng, Q. Liu, H. Lv, J. Suñé, M. Liu, *Nanoscale Res. Lett.* **2015**, *10*, 420.
[19] W. Xue, S. Gao, J. Shang, X. Yi, G. Liu, R. Li, *Adv. Electron. Mater.* **2019**, *5*, 1800854.
[20] B. J. Van Wees, H. Van Houten, C. W. J. Beenakker, J. G. Williamson, L. P. Kouwenhoven, D. Van Der Marel, C. T. Foxon, *Phys. Rev. Lett.* **1988**, *60*, 848.

[21] D. A. Wharam, T. J. Thornton, R. Newbury, M. Pepper, H. Ahmed, J. E. F. Frost, D. G. Hasko, D. C. Peacock, D. A. Ritchie, G. A. C. Jones, *J. Phys. C: Solid State Phys.* **1988**, *21*, L209.
[22] C. W. J. Beenakker, H. van Houten, in *Solid State Physics*, Vol. *44*, (Eds: H. Ehrenreich, D. Turnbull), Elsevier, Amsterdam, The Netherlands **1991**, p. 1.
[23] E. A. Montie, E. C. Cosman, G. W. 't Hooft, M. B. van der Mark, C. W. J. Beenakker, *Nature* **1991**, *350*, 594.
[24] H. van Houten, C. Beenakker, *Phys. Today* **1996**, *49*, 22.
[25] A. Tsukazaki, A. Ohtomo, T. Kita, Y. Ohno, H. Ohno, M. Kawasaki, *Science* **2007**, *315*, 1388.
[26] A. Ron, Y. Dagan, *Phys. Rev. Lett.* **2014**, *112*, 136801.
[27] N. Tombros, A. Veligura, J. Junesch, M. H. D. Guimarães, I. J. Vera-Marun, H. T. Jonkman, B. J. van Wees, *Nat. Phys.* **2011**, *7*, 697.
[28] J. M. van Ruitenbeek, A. Alvarez, I. Piñeyro, C. Grahmann, P. Joyez, M. H. Devoret, D. Esteve, C. Urbina, *Rev. Sci. Instrum.* **1996**, *67*, 108.
[29] J. M. Krans, J. M. van Ruitenbeek, V. V. Fisun, I. K. Yanson, L. J. de Jongh, *Nature* **1995**, *375*, 767.
[30] E. Scheer, N. Agraït, J. C. Cuevas, A. L. Yeyati, B. Ludoph, A. Martín-Rodero, G. R. Bollinger, J. M. van Ruitenbeek, C. Urbina, *Nature* **1998**, *394*, 154.
[31] N. Agraït, J. G. Rodrigo, S. Vieira, *Phys. Rev. B* **1993**, *47*, 12345.
[32] J. I. Pascual, J. Mendez, J. Gomez-Herrero, A. M. Baro, N. Garcia, U. Landman, W. D. Luedtke, E. N. Bogachek, H. P. Cheng, *Science* **1995**, *267*, 1793.
[33] A. Geresdi, A. Halbritter, A. Gyenis, P. Makk, G. Mihály, *Nanoscale* **2011**, *3*, 1504.
[34] H. Ohnishi, Y. Kondo, K. Takayanagi, *Nature* **1998**, *395*, 780.
[35] C. Z. Li, N. J. Tao, *Appl. Phys. Lett.* **1998**, *72*, 894.
[36] C. Z. Li, A. Bogozi, W. Huang, N. J. Tao, *Nanotechnology* **1999**, *10*, 221.
[37] K. Terabe, T. Hasegawa, T. Nakayama, M. Aono, *RIKEN Rev.* **2001**, *37*, 7.
[38] K. Terabe, T. Hasegawa, T. Nakayama, M. Aono, *Nature* **2005**, *433*, 47.
[39] R. Waser, *Nanoelectronics and Information Technology: Materials, Processes, Devices*, John Wiley & Sons, New York **2012**.
[40] S. Tappertzhofen, I. Valov, R. Waser, *Nanotechnology* **2012**, *23*, 145703.
[41] H. Lv, X. Xu, H. Liu, R. Liu, Q. Liu, W. Banerjee, H. Sun, S. Long, L. Li, M. Liu, *Sci. Rep.* **2015**, *5*, 7764.
[42] M. Lübben, I. Valov, *Adv. Electron. Mater.* **2019**, *5*, 1800933.
[43] Z. Wang, H. Jiang, M. Hyung Jang, P. Lin, A. Ribbe, Q. Xia, J. J. Yang, *Nanoscale* **2016**, *8*, 14023.
[44] J. H. Yoon, J. Zhang, P. Lin, N. Upadhyay, P. Yan, Y. Liu, Q. Xia, J. J. Yang, *Adv. Mater.* **2020**, *32*, 1904599.
[45] Y. Yang, P. Gao, L. Li, X. Pan, S. Tappertzhofen, S. Choi, R. Waser, I. Valov, W. D. Lu, *Nat. Commun.* **2014**, *5*, 4232.
[46] S. Tappertzhofen, I. Valov, T. Tsuruoka, T. Hasegawa, R. Waser, M. Aono, *ACS Nano* **2013**, *7*, 6396.
[47] T. Tsuruoka, K. Terabe, T. Hasegawa, I. Valov, R. Waser, M. Aono, *Adv. Funct. Mater.* **2012**, *22*, 70.
[48] M. Lübben, S. Menzel, S. G. Park, M. Yang, R. Waser, I. Valov, *Nanotechnology* **2017**, *28*, 135205.
[49] M. Lübben, F. Cüppers, J. Mohr, M. von Witzleben, U. Breuer, R. Waser, C. Neumann, I. Valov, *Sci. Adv.* **2020**, *6*, eaaz9079.
[50] D.-Y. Cho, S. Tappertzhofen, R. Waser, I. Valov, *Nanoscale* **2013**, *5*, 1781.
[51] I. Valov, T. Tsuruoka, *J. Phys. D: Appl. Phys.* **2018**, *51*, 413001.
[52] I. Valov, *Semicond. Sci. Technol.* **2017**, *32*, 093006,
[53] W. Chen, S. Tappertzhofen, H. J. Barnaby, M. N. Kozicki, *J. Electroceram.* **2017**, *39*, 109.
[54] A. Wedig, M. Luebben, D.-Y. Cho, M. Moors, K. Skaja, V. Rana, T. Hasegawa, K. K. Adepalli, B. Yildiz, R. Waser, I. Valov, *Nat. Nanotechnol.* **2016**, *11*, 67.
[55] M. Lübben, P. Karakolis, V. Ioannou-Sougleridis, P. Normand, P. Dimitrakis, I. Valov, *Adv. Mater.* **2015**, *27*, 6202.
[56] I. Valov, *ChemElectroChem* **2014**, *1*, 26.
[57] D.-H. Kwon, K. M. Kim, J. H. Jang, J. M. Jeon, M. H. Lee, G. H. Kim, X.-S. Li, G.-S. Park, B. Lee, S. Han, M. Kim, C. S. Hwang, *Nat. Nanotechnol.* **2010**, *5*, 148.
[58] S. Long, X. Lian, C. Cagli, X. Cartoixà, R. Rurali, E. Miranda, D. Jiménez, L. Perniola, M. Liu, J. Suñé, *Appl. Phys. Lett.* **2013**, *102*, 183505.
[59] I. Valov, G. Staikov, *J. Solid State Electrochem.* **2013**, *17*, 365.
[60] I. Valov, E. Linn, S. Tappertzhofen, S. Schmelzer, J. van den Hurk, F. Lentz, R. Waser, *Nat. Commun.* **2013**, *4*, 1771.
[61] B. V. W. H. Van Houten, C. Beenakker, K. Ensslin, *Quantum Point Contacts*, Academic Press, San Diego, CA, USA **1992**.
[62] P. A. Mello, N. Kumar, *Quantum Transport in Mesoscopic Systems*, Oxford University Press, Oxford, UK **2004**.
[63] P. Sheng, *Introduction to Wave Scattering, Localization, and Mesoscopic Phenomena*, Springer, Berlin, Germany **2006**.
[64] S. Datta, *Lessons from Nanoelectronics: A New Perspective on Transport*, World Scientific, Singapore **2012**.
[65] T. Ihn, *Semiconductor Nanostructures Quantum States and Electronic Transport*, Oxford University Press, Oxford, UK **2010**.
[66] D. Gall, *J. Appl. Phys.* **2016**, *119*, 085101.
[67] R. Landauer, *IBM J. Res. Dev.* **1957**, *1*, 223.
[68] M. Büttiker, *Phys. Rev. Lett.* **1986**, *57*, 1761.
[69] J. C. Maxwell, *A Treatise on Electricity and Magnetism*, Dover Publication Inc, Mineola, NY, USA **1954**.
[70] Y. V. Sharvin, *Sov. Phys. JETP* **1965**, *21*, 655.
[71] N. Agraït, *Phys. Rep.* **2003**, *377*, 81.
[72] Y. Imry, in *Directions in Condensed Matter Physics* (Eds: G. Grinstein, G. Mazenko), World Scientific, Singapore **1986**, pp. 101–163.
[73] T. Ando, Y. Arakawa, K. Furuya, S. Komiyama, H. Nakashima, *Mesoscopic Physics and Electronics*, Springer-Verlag, Berlin, Germany, **1998**.
[74] P. Hu, *Phys. Rev. B* **1987**, *35*, 4078.
[75] E. Miranda, J. Sune, in *39th Annu. 2001 IEEE Int. Reliability Physics Symp. Proc. (Cat. No.00CH37167)*, 39th Annual (Cat. No. 00CH37167), IEEE, Piscataway, NJ, USA **2001**, pp. 367–379.
[76] E. Miranda, J. Suñé, *Microelectron. Reliab.* **2004**, *44*, 1.
[77] M. Büttiker, *Phys. Rev. B* **1990**, *41*, 7906.
[78] E. A. Miranda, C. Walczyk, C. Wenger, T. Schroeder, *IEEE Electron Device Lett.* **2010**, *31*, 609.
[79] E. Miranda, D. Jimenez, J. Sune, *IEEE Electron Device Lett.* **2012**, *33*, 1474.
[80] L. P. Kouwenhoven, B. J. van Wees, C. J. P. M. Harmans, J. G. Williamson, H. van Houten, C. W. J. Beenakker, C. T. Foxon, J. J. Harris, *Phys. Rev. B* **1989**, *39*, 8040.
[81] E. Miranda, S. Kano, C. Dou, K. Kakushima, J. Suñé, H. Iwai, *Appl. Phys. Lett.* **2012**, *101*, 012910.
[82] A. Mehonic, A. Vrajitoarea, S. Cueff, S. Hudziak, H. Howe, C. Labbé, R. Rizk, M. Pepper, A. J. Kenyon, *Sci. Rep.* **2013**, *3*, 2708.
[83] S. Petzold, E. Piros, R. Eilhardt, A. Zintler, T. Vogel, N. Kaiser, A. Radetinac, P. Komissinskiy, E. Jalaguier, E. Nolot, C. Charpin-Nicolle, C. Wenger, L. Molina-Luna, E. Miranda, L. Alff, *Adv. Electron. Mater.* **2020**, *6*, 2000439.
[84] F. Pauly, M. Dreher, J. K. Viljas, M. Häfner, J. C. Cuevas, P. Nielaba, *Phys. Rev. B* **2006**, *74*, 235106.
[85] J. van Ruitenbeek, M. Morales Masis, E. Miranda, in *Resistive Switching: From Fundamentals of Nanoionic Redox Processes to Memristive Device Applications* (Eds: D. Ielmini, R. Waser), Wiley-VCH, Weinheim, Germany **2016**, p. 197.

[86] J. J. T. Wagenaar, M. Morales-Masis, J. M. van Ruitenbeek, *J. Appl. Phys.* **2012**, *111*, 014302.
[87] K. L. Chopra, *Proc. IEEE* **1963**, *51*, 941.
[88] W. R. Hiatt, T. W. Hickmott, *Appl. Phys. Lett.* **1965**, *6*, 106.
[89] D. Kahng, S. M. Sze, *Bell Syst. Tech. J.* **1967**, *46*, 1288.
[90] R. Bez, E. Camerlenghi, A. Modelli, A. Visconti, *Proc. IEEE* **2003**, *91*, 489.
[91] D. Ielmini, *Microelectron. Eng.* **2009**, *86*, 1870.
[92] M. Kozicki, M. Mitkova, M. Park, M. Balakrishnan, C. Gopalan, *Superlattices Microstruct.* **2003**, *34*, 459.
[93] M. N. Kozicki, M. Balakrishnan, C. Gopalan, C. Ratnakumar, M. Mitkova, in *Symp. Non-Volatile Memory Technology 2005*, IEEE, Piscataway, NJ, USA **2005**, pp. 83–89.
[94] M. N. Kozicki, C. Gopalan, M. Balakrishnan, M. Park, M. Mitkova, in *Proc. 2004 IEEE Computational Systems Bioinformatics Conf.*, IEEE, Piscataway, NJ, USA **2004**, pp. 10–17.
[95] I. Valov, M. N. Kozicki, *J. Phys. D.: Appl. Phys.* **2013**, *46*, 074005.
[96] K. Szot, W. Speier, G. Bihlmayer, R. Waser, *Nat. Mater.* **2006**, *5*, 312.
[97] M. Aono, T. Hasegawa, *Proc. IEEE* **2010**, *98*, 2228.
[98] X. Zhong, I. Rungger, P. Zapol, O. Heinonen, *Phys. Rev. B* **2016**, *94*, 165160.
[99] V. K. Sahu, P. Misra, A. K. Das, R. S. Ajimsha, B. Singh, *AIP Conf. Proc.* **2017**, *1832*, 120026.
[100] L. Jiang, L. Xu, J. W. Chen, P. Yan, K. H. Xue, H. J. Sun, X. S. Miao, *Appl. Phys. Lett.* **2016**, *109*, 153506.
[101] J. R. Jameson, N. Gilbert, F. Koushan, J. Saenz, J. Wang, S. Hollmer, M. Kozicki, N. Derhacobian, *IEEE Electron Device Lett.* **2012**, *33*, 257.
[102] S. Tappertzhofen, E. Linn, S. Menzel, A. J. Kenyon, R. Waser, I. Valov, *IEEE Trans. Nanotechnol.* **2015**, *14*, 505.
[103] S. R. Nandakumar, M. Minvielle, S. Nagar, C. Dubourdieu, B. Rajendran, *Nano Lett.* **2016**, *16*, 1602.
[104] S. Gao, C. Chen, Z. Zhai, H. Y. Liu, Y. S. Lin, S. Z. Li, S. H. Lu, G. Y. Wang, C. Song, F. Zeng, F. Pan, *Appl. Phys. Lett.* **2014**, *105*, 063504.
[105] T. Tsuruoka, T. Hasegawa, K. Terabe, M. Aono, *Nanotechnology* **2012**, *23*, 435705.
[106] F. G. Aga, J. Woo, J. Song, J. Park, S. Lim, C. Sung, H. Hwang, *Nanotechnology* **2017**, *28*, 115707.
[107] W. Banerjee, H. Hwang, *Adv. Electron. Mater.* **2019**, *5*, 1900744.
[108] J. Zhao, Z. Zhou, Y. Zhang, J. Wang, L. Zhang, X. Li, M. Zhao, H. Wang, Y. Pei, Q. Zhao, Z. Xiao, K. Wang, C. Qin, G. Wang, H. Li, B. Ding, F. Yan, K. Wang, D. Ren, B. Liu, X. Yan, *J. Mater. Chem. C* **2019**, *7*, 1298.
[109] S. Gao, F. Zeng, C. Chen, G. Tang, Y. Lin, Z. Zheng, C. Song, F. Pan, *Nanotechnology* **2013**, *24*, 335201.
[110] K. Krishnan, M. Muruganathan, T. Tsuruoka, H. Mizuta, M. Aono, *Adv. Funct. Mater.* **2017**, *27*, 1605104.
[111] X. Zhao, H. Xu, Z. Wang, L. Zhang, J. Ma, Y. Liu, *Carbon* **2015**, *91*, 38.
[112] Y. Kang, H. Ruan, R. O. Claus, J. Heremans, M. Orlowski, *Nanoscale Res. Lett.* **2016**, *11*, 179.
[113] X. Zhao, J. Xu, D. Xie, Z. Wang, H. Xu, Y. Lin, J. Hu, Y. Liu, *Adv. Mater.* **2021**, *33*, 2104023.
[114] M. Kozicki, M. Yun, S.-J. Yang, J. Aberouette, J. Bird, *Superlattices Microstruct.* **2000**, *27*, 485.
[115] J. Sune, E. Miranda, M. Nafria, X. Aymerich, in *Int. Electron Devices Meeting 1998: Tech. Dig. (Cat. No. 98CH36217)*, IEEE, Piscataway, NJ, USA **1998**, pp. 191–194.
[116] Y.-E. Syu, T.-C. Chang, J.-H. Lou, T.-M. Tsai, K.-C. Chang, M.-J. Tsai, Y.-L. Wang, M. Liu, S. M. Sze, *Appl. Phys. Lett.* **2013**, *102*, 172903.
[117] M.-H. Peng, C.-Y. Pan, H.-X. Zheng, T.-C. Chang, P. Jiang, *ACS. Appl. Nano Mater.* **2021**, *4*, 11296.
[118] X. Zhu, W. Su, Y. Liu, B. Hu, L. Pan, W. Lu, J. Zhang, R.-W. Li, *Adv. Mater.* **2012**, *24*, 3941.
[119] Y. Wang, X. Qian, K. Chen, Z. Fang, W. Li, J. Xu, *Appl. Phys. Lett.* **2013**, *102*, 042103.
[120] Y. Nishi, H. Sasakura, T. Kimoto, *J. Mater. Res.* **2017**, *32*, 2631.
[121] C. Hu, M. D. McDaniel, A. Posadas, A. A. Demkov, J. G. Ekerdt, E. T. Yu, *Nano Lett.* **2014**, *14*, 4360.
[122] C. Hu, M. D. McDaniel, J. G. Ekerdt, E. T. Yu, *IEEE Electron Device Lett.* **2013**, *34*, 1385.
[123] J. Ge, M. Chaker, *ACS Appl. Mater. Interfaces* **2017**, *9*, 16327.
[124] Z. Xie, S. Gao, X. Ye, H. Yang, G. Gong, Y. Lu, J. Ye, G. Liu, R. Li, *Phys. Chem. Chem. Phys.* **2020**, *22*, 26322.
[125] W. Yi, S. E. Savel'ev, G. Medeiros-Ribeiro, F. Miao, M.-X. Zhang, J. J. Yang, A. M. Bratkovsky, R. S. Williams, *Nat. Commun.* **2016**, *7*, 11142.
[126] Q. Duan, J. Li, J. Zhu, T. Zhang, J. Yang, Y. Yang, R. Huang, in *2019 China Semiconductor Technology Int. Conf.*, IEEE, Piscataway, NJ, USA **2019**, https://doi.org/10.1109/CSTIC.2019.8755752.
[127] Y. Nishi, *MRS Adv.* **2021**, *6*, 554.
[128] T. N. Török, M. Csontos, P. Makk, A. Halbritter, *Nano Lett.* **2020**, *20*, 1192.
[129] C. Schirm, M. Matt, F. Pauly, J. C. Cuevas, P. Nielaba, E. Scheer, *Nat. Nanotechnol.* **2013**, *8*, 645.
[130] B. Ludoph, J. M. Van Ruitenbeek, *Phys. Rev. B* **2000**, *61*, 2273.
[131] S. Deswal, R. R. Malode, A. Kumar, A. Kumar, *RSC Adv.* **2019**, *9*, 9494.
[132] Q. Chen, G. Liu, W. Xue, J. Shang, S. Gao, X. Yi, Y. Lu, X. Chen, M. Tang, X. Zheng, R.-W. Li, *ACS Appl. Electron. Mater.* **2019**, *1*, 789.
[133] S. Tappertzhofen, E. Linn, U. Bottger, R. Waser, I. Valov, *IEEE Electron Device Lett.* **2014**, *35*, 208.
[134] H. Jiang, D. Belkin, S. E. Savel'Ev, S. Lin, Z. Wang, Y. Li, S. Joshi, R. Midya, C. Li, M. Rao, M. Barnell, Q. Wu, J. J. Yang, Q. Xia, S. E. Savel'ev, S. Lin, Z. Wang, Y. Li, S. Joshi, R. Midya, C. Li, M. Rao, M. Barnell, Q. Wu, J. J. Yang, Q. Xia, *Nat. Commun.* **2017**, *8*, 882.
[135] X. Li, T. Zanotti, T. Wang, K. Zhu, F. M. Puglisi, M. Lanza, *Adv. Funct. Mater.* **2021**, *31*, 2102172.
[136] D. Ielmini, F. Nardi, C. Cagli, *Appl. Phys. Lett.* **2010**, *96*, 2.
[137] M. J. Uren, D. J. Day, M. J. Kirton, *Appl. Phys. Lett.* **1985**, *47*, 1195.
[138] K. K. Hung, P. K. Ko, C. Hu, Y. C. Cheng, *IEEE Electron Device Lett.* **1990**, *11*, 90.
[139] J. P. Campbell, J. Qin, K. P. Cheung, L. C. Yu, J. S. Suehle, A. Oates, K. Sheng, in *2009 IEEE Int. Reliability Physics Symp.*, IEEE, Piscataway, NJ, USA **2009**, pp. 382–388.
[140] B. Sánta, Z. Balogh, L. Pósa, D. Krisztián, T. N. Török, D. Molnár, C. Sinkó, R. Hauert, M. Csontos, A. Halbritter, *ACS Appl. Mater. Interfaces* **2021**, *13*, 7453.
[141] S. Brivio, J. Frascaroli, E. Covi, S. Spiga, *Sci. Rep.* **2019**, *9*, 6310.
[142] R. Tolley, A. Silvidi, C. Little, K. F. Eid, *Am. J. Phys.* **2013**, *81*, 14.
[143] C. Chen, S. Gao, F. Zeng, G. Y. Wang, S. Z. Li, C. Song, F. Pan, *Appl. Phys. Lett.* **2013**, *103*, 043510.
[144] S. I. Kim, J. H. Lee, Y. W. Chang, S. S. Hwang, K.-H. Yoo, *Appl. Phys. Lett.* **2008**, *93*, 033503.
[145] G. Milano, S. Porro, I. Valov, C. Ricciardi, *Adv. Electron. Mater.* **2019**, *5*, 1800909.
[146] G. Milano, M. Luebben, Z. Ma, R. Dunin-Borkowski, L. Boarino, C. F. Pirri, R. Waser, C. Ricciardi, I. Valov, *Nat. Commun.* **2018**, *9*, 5151.
[147] G. Milano, L. Boarino, C. Ricciardi, *Nanotechnology* **2019**, *30*, 244001.
[148] G. Milano, F. Raffone, M. Luebben, L. Boarino, G. Cicero, I. Valov, C. Ricciardi, *ACS Appl. Mater. Interfaces* **2020**, *12*, 48773.
[149] E. Miranda, G. Milano, C. Ricciardi, *IEEE Trans. Nanotechnol.* **2020**, *19*, 297.
[150] E. Miranda, G. Milano, C. Ricciardi, *IEEE Trans. Nanotechnol.* **2020**, *19*, 609.

[151] S. L. Johnson, A. Sundararajan, D. P. Hunley, D. R. Strachan, *Nanotechnology* **2010**, *21*, 125204.
[152] R. Böckle, M. Sistani, P. Staudinger, M. S. Seifner, S. Barth, A. Lugstein, *Nanotechnology* **2020**, *31*, 445204.
[153] A. Vokhmintsev, I. Petrenyov, R. Kamalov, I. Weinstein, *Nanotechnology* **2022**, *33*, 075208.
[154] A. Younis, D. Chu, S. Li, *J. Mater. Chem. C* **2014**, *2*, 10291.
[155] H. G. Manning, F. Niosi, C. G. da Rocha, A. T. Bellew, C. O'Callaghan, S. Biswas, P. F. Flowers, B. J. Wiley, J. D. Holmes, M. S. Ferreira, J. J. Boland, *Nat. Commun.* **2018**, *9*, 3219.
[156] G. Milano, G. Pedretti, M. Fretto, L. Boarino, F. Benfenati, D. Ielmini, I. Valov, C. Ricciardi, *Adv. Intell. Syst.* **2020**, *2*, 2000096.
[157] J. Hochstetter, R. Zhu, A. Loeffler, A. Diaz-Alvarez, T. Nakayama, Z. Kuncic, *Nat. Commun.* **2021**, *12*, 4008.
[158] A. Z. Stieg, A. V. Avizienis, H. O. Sillin, C. Martin-Olmos, M. Aono, J. K. Gimzewski, *Adv. Mater.* **2012**, *24*, 286.
[159] S. Lilak, W. Woods, K. Scharnhorst, C. Dunham, C. Teuscher, A. Z. Stieg, *J. K. Gimzewski, Front. Nanotechnol.* **2021**, *3*, 675792.
[160] Z. Kuncic, T. Nakayama, *Adv. Phys. X* **2021**, *6*, 1894234.
[161] G. Milano, G. Pedretti, K. Montano, S. Ricci, S. Hashemkhani, L. Boarino, D. Ielmini, C. Ricciardi, *Nat. Mater.* **2022**, *21*, 195.
[162] Q. Li, A. Diaz-Alvarez, R. Iguchi, J. Hochstetter, A. Loeffler, R. Zhu, Y. Shingaya, Z. Kuncic, K. Uchida, T. Nakayama, *Adv. Funct. Mater.* **2020**, *30*, 2003679.
[163] S. Bose, S. Shirai, J. Mallinson, S. Acharya, E. Galli, S. Brown, in *2018 IEEE 18th Int. Conf. on Nanotechnology (IEEE-NANO)*, IEEE, Piscataway, NJ, USA **2018**, https://doi.org/10.1109/NANO.2018.8626230.
[164] S. K. Bose, J. B. Mallinson, R. M. Gazoni, S. A. Brown, *IEEE Trans. Electron Devices* **2017**, *64*, 5194.
[165] K. S. Novoselov, A. K. Geim, S. V. Morozov, D. Jiang, Y. Zhang, S. V. V. Dubonos, I. V. V. Grigorieva, A. A. A. Firsov, *Science* **2004**, *306*, 666.
[166] Y. Yi, Z. Chen, X. Yu, Z. Zhou, J. Li, *Adv. Quantum Technol.* **2019**, *2*, 1800111.
[167] F. Hui, E. Grustan-Gutierrez, S. Long, Q. Liu, A. K. Ott, A. C. Ferrari, M. Lanza, *Adv. Electron. Mater.* **2017**, *3*, 1600195.
[168] C. L. He, F. Zhuge, X. F. Zhou, M. Li, G. C. Zhou, Y. W. Liu, J. Z. Wang, B. Chen, W. J. Su, Z. P. Liu, Y. H. Wu, P. Cui, R.-W. Li, *Appl. Phys. Lett.* **2009**, *95*, 232101.
[169] R. Ge, X. Wu, M. Kim, J. Shi, S. Sonde, L. Tao, Y. Zhang, J. C. Lee, D. Akinwande, *Nano Lett.* **2018**, *18*, 434.
[170] V. K. Sangwan, H.-S. Lee, H. Bergeron, I. Balla, M. E. Beck, K.-S. Chen, M. C. Hersam, *Nature* **2018**, *554*, 500.
[171] R. Xu, H. Jang, M.-H. Lee, D. Amanov, Y. Cho, H. Kim, S. Park, H. Shin, D. Ham, *Nano Lett.* **2019**, *19*, 2411.
[172] W. Huh, D. Lee, C. Lee, *Adv. Mater.* **2020**, *32*, 2002092.
[173] S. Hao, X. Ji, S. Zhong, K. Y. Pang, K. G. Lim, T. C. Chong, R. Zhao, *Adv. Electron. Mater.* **2020**, *6*, 1901335.
[174] K. Zhu, X. Liang, B. Yuan, M. A. Villena, C. Wen, T. Wang, S. Chen, F. Hui, Y. Shi, M. Lanza, *ACS Appl. Mater. Interfaces* **2019**, *11*, 37999.
[175] R. D. Nikam, K. G. Rajput, H. Hwang, *Small* **2021**, *17*, 2006760.
[176] X. Zhang, H. Xie, Z. Liu, C. Tan, Z. Luo, H. Li, J. Lin, L. Sun, W. Chen, Z. Xu, L. Xie, W. Huang, H. Zhang, *Angew. Chem., Int. Ed.* **2015**, *54*, 3653.
[177] F. Rahman, T. Ahmed, S. Walia, E. Mayes, S. Sriram, M. Bhaskaran, S. Balendhran, *Nanoscale* **2018**, *10*, 19711.
[178] M. Wang, S. Cai, C. Pan, C. Wang, X. Lian, Y. Zhuo, K. Xu, T. Cao, X. Pan, B. Wang, S. J. Liang, J. J. Yang, P. Wang, F. Miao, *Nat. Electron.* **2018**, *1*, 130.
[179] A. Krishnaprasad, N. Choudhary, S. Das, D. Dev, H. Kalita, H.-S. Chung, O. Aina, Y. Jung, T. Roy, *Appl. Phys. Lett.* **2019**, *115*, 103104.
[180] L. Zhang, T. Gong, H. Wang, Z. Guo, H. Zhang, *Nanoscale* **2019**, *11*, 12413.
[181] M. Lanza, Q. Smets, C. Huyghebaert, L.-J. Li, *Nat. Commun.* **2020**, *11*, 5689.
[182] B. Standley, W. Bao, H. Zhang, J. Bruck, C. N. Lau, M. Bockrath, *Nano Lett.* **2008**, *8*, 3345.
[183] C. Pan, E. Miranda, M. A. Villena, N. Xiao, X. Jing, X. Xie, T. Wu, F. Hui, Y. Shi, M. Lanza, *2D Mater.* **2017**, *4*, 025099.
[184] J. Lee, W. D. Lu, *Adv. Mater.* **2018**, *30*, 1702770.
[185] F. Miao, J. P. Strachan, J. J. Yang, M. X. Zhang, I. Goldfarb, A. C. Torrezan, P. Eschbach, R. D. Kelley, G. Medeiros-Ribeiro, R. S. Williams, *Adv. Mater.* **2011**, *23*, 5633.
[186] K. Kado, M. Uenuma, K. Sharma, H. Yamazaki, S. Urakawa, Y. Ishikawa, Y. Uraoka, *Appl. Phys. Lett.* **2014**, 105, 123506.
[187] I. Valov, I. Sapezanskaia, A. Nayak, T. Tsuruoka, T. Bredow, T. Hasegawa, G. Staikov, M. Aono, R. Waser, *Nat. Mater.* **2012**, *11*, 530.
[188] U. Celano, L. Goux, K. Opsomer, A. Belmonte, M. Iapichino, C. Detavernier, M. Jurczak, W. Vandervorst, *Nanoscale* **2013**, *5*, 11187.
[189] Y. Du, A. Kumar, H. Pan, K. Zeng, S. Wang, P. Yang, A. T. S. Wee, *AIP Adv.* **2013**, *3*, 082107.
[190] Y. Hirose, H. Hirose, *J. Appl. Phys.* **1976**, *47*, 2767.
[191] Y. Hayakawa, A. Himeno, R. Yasuhara, W. Boullart, E. Vecchio, T. Vandeweyer, T. Witters, D. Crotti, M. Jurczak, S. Fujii, S. Ito, Y. Kawashima, Y. Ikeda, A. Kawahara, K. Kawai, Z. Wei, S. Muraoka, K. Shimakawa, T. Mikawa, S. Yoneda, in *2015 Symp. on VLSI Technology (VLSI Technology)*, IEEE, Piscataway, NJ, USA **2015**, pp. T14–T15.
[192] M. N. Kozicki, M. Mitkova, *J. Non-Cryst. Solids* **2006**, *352*, 567.
[193] C. Rossel, G. I. Meijer, D. Brémaud, D. Widmer, *J. Appl. Phys.* **2001**, *90*, 2892.
[194] W. Guan, S. Long, Q. Liu, M. Liu, W. Wang, *IEEE Electron Device Lett.* **2008**, *29*, 434.
[195] W. A. Hubbard, A. Kerelsky, G. Jasmin, E. R. White, J. Lodico, M. Mecklenburg, B. C. Regan, *Nano Lett.* **2015**, *15*, 3983.
[196] C. Li, B. Gao, Y. Yao, X. Guan, X. Shen, Y. Wang, P. Huang, L. Liu, X. Liu, J. Li, C. Gu, J. Kang, R. Yu, *Adv. Mater.* **2017**, *29*, 1602976.
[197] M. T. McDowell, K. L. Jungjohann, U. Celano, *Nano Lett.* **2018**, *18*, 657.
[198] D. Cooper, C. Baeumer, N. Bernier, A. Marchewka, C. La Torre, R. E. Dunin-Borkowski, S. Menzel, R. Waser, R. Dittmann, *Adv. Mater.* **2017**, *29*, 1700212.
[199] Y. Yang, R. Huang, *Nat. Electron.* **2018**, *1*, 274.
[200] W. A. Hubbard, J. J. Lodico, H. L. Chan, M. Mecklenburg, B. C. Regan, *Adv. Funct. Mater.* **2022**, *32*, 2102313.
[201] M. N. Kozicki, C. Gopalan, M. Balakrishnan, M. Mitkova, *IEEE Trans. Nanotechnol.* **2006**, *5*, 535.
[202] R. Yasuhara, K. Fujiwara, K. Horiba, H. Kumigashira, M. Kotsugi, M. Oshima, H. Takagi, *Appl. Phys. Lett.* **2009**, *95*, 012110.
[203] G.-S. Park, Y. B. Kim, S. Y. Park, X. S. Li, S. Heo, M.-J. Lee, M. Chang, J. H. Kwon, M. Kim, U.-I. Chung, R. Dittmann, R. Waser, K. Kim, *Nat. Commun.* **2013**, *4*, 2382.
[204] K. Szot, R. Dittmann, W. Speier, R. Waser, *Phys. Status Solidi - Rapid Res. Lett.* **2007**, *1*, R86.
[205] Y.-M. Kim, J. Lee, D.-J. Jeon, S.-E. Oh, J.-S. Yeo, *Appl. Microsc.* **2021**, *51*, 7.
[206] Y. Hou, U. Celano, L. Goux, L. Liu, R. Degraeve, Y. Cheng, J. Kang, M. Jurczak, W. Vandervorst, *Appl. Phys. Lett.* **2016**, *109*, 023508.
[207] J. Song, Y. Zhou, B. D. Huey, *Appl. Phys. Lett.* **2021**, *118*, 080501.
[208] U. Celano, L. Goux, A. Belmonte, K. Opsomer, A. Franquet, A. Schulze, C. Detavernier, O. Richard, H. Bender, M. Jurczak, W. Vandervorst, *Nano Lett.* **2014**, *14*, 2401.
[209] U. Celano, G. Giammaria, L. Goux, A. Belmonte, M. Jurczak, W. Vandervorst, *Nanoscale* **2016**, *8*, 13915.
[210] U. Celano, L. Goux, R. Degraeve, A. Fantini, O. Richard, H. Bender, M. Jurczak, W. Vandervorst, *Nano Lett.* **2015**, *15*, 7970.

[211] W. Vandervorst, C. Fleischmann, J. Bogdanowicz, A. Franquet, U. Celano, K. Paredis, A. Budrevich, *Mater. Sci. Semicond. Process.* **2017**, *62*, 31.
[212] B.-G. Chae, J.-B. Seol, J.-H. Song, K. Baek, S.-H. Oh, H. Hwang, C.-G. Park, *Adv. Mater.* **2017**, *29*, 1701752.
[213] X. Guo, C. Schindler, S. Menzel, R. Waser, *Appl. Phys. Lett.* **2007**, *91*, 133513.
[214] J. P. Strachan, D. B. Strukov, J. Borghetti, J. Joshua Yang, G. Medeiros-Ribeiro, R. Stanley Williams, *Nanotechnology* **2011**, *22*, 254015.
[215] D. T. Schoen, A. L. Holsteen, M. L. Brongersma, *Nat. Commun.* **2016**, *7*, 12162.
[216] U. Celano, K. Paredis, A. Humphris, M. Tedaldi, C. O'sullivan, P. Hole, J. Goulden, *Proc. SPIE* **2021**, *11611*, 116110J.
[217] S. Pi, C. Li, H. Jiang, W. Xia, H. Xin, J. J. Yang, Q. Xia, *Nat. Nanotechnol.* **2019**, *14*, 35.
[218] C. Li, L. Han, H. Jiang, M. H. Jang, P. Lin, Q. Wu, M. Barnell, J. J. Yang, H. L. Xin, Q. Xia, *Nat. Commun.* **2017**, *8*, 15666.
[219] B. K. You, J. M. Kim, D. J. Joe, K. Yang, Y. Shin, Y. S. Jung, K. J. Lee, *ACS Nano* **2016**, *10*, 9478.
[220] Y. Li, J. Tang, B. Gao, W. Sun, Q. Hua, W. Zhang, X. Li, W. Zhang, H. Qian, H. Wu, *Adv. Sci.* **2020**, *7*, 2002251.
[221] R. Midya, Z. Wang, J. Zhang, S. E. Savel'ev, C. Li, M. Rao, M. H. Jang, S. Joshi, H. Jiang, P. Lin, K. Norris, N. Ge, Q. Wu, M. Barnell, Z. Li, H. L. Xin, R. S. Williams, Q. Xia, J. J. Yang, *Adv. Mater.* **2017**, *29*, 1604457.
[222] M. Jerry, A. Aziz, K. Ni, S. Datta, S. K. Gupta, N. Shukla, in *2018 IEEE Symp. on VLSI Technology*, IEEE, Piscataway, NJ, USA **2018**, pp. 129–130.
[223] W. Cheng, R. Liang, Q. Hua, Z. Zhuo, W. Chen, S. Zhang, Y. Liu, L. Zhao, J. Xu, *Appl. Phys. Express* **2019**, *12*, 091002.
[224] T. Ibrayev, I. Fedorova, A. K. Maan, A. P. James, *Circuits Syst.* **2014**, *05*, 265.
[225] Y. S. Kim, M. W. Son, H. Song, J. Park, J. An, J. B. Jeon, G. Y. Kim, S. Son, K. M. Kim, *Adv. Intell. Syst.* **2020**, *2*, 1900156.
[226] N. Xu, T. Park, K. J. Yoon, C. S. Hwang, *Phys. Status Solidi - Rapid Res. Lett.* **2021**, *15*, 2100208.
[227] T. Ohno, T. Hasegawa, T. Tsuruoka, K. Terabe, J. K. Gimzewski, M. Aono, *Nat. Mater.* **2011**, *10*, 591.
[228] L. Jiang, F.-C. Lv, R. Yang, D.-C. Hu, X. Guo, *J. Mater.* **2019**, *5*, 296.
[229] Q. Chen, T. Han, M. Tang, Z. Zhang, X. Zheng, G. Liu, *Micromachines* **2020**, *11*, 427.
[230] H. Yeon, P. Lin, C. Choi, S. H. Tan, Y. Park, D. Lee, J. Lee, F. Xu, B. Gao, H. Wu, H. Qian, Y. Nie, S. Kim, J. Kim, *Nat. Nanotechnol.* **2020**, *15*, 574.
[231] Z. Wang, S. Joshi, S. Savel'ev, W. Song, R. Midya, Y. Li, M. Rao, P. Yan, S. Asapu, Y. Zhuo, H. Jiang, P. Lin, C. Li, J. H. Yoon, N. K. Upadhyay, J. Zhang, M. Hu, J. P. Strachan, M. Barnell, Q. Wu, H. Wu, R. S. Williams, Q. Xia, J. J. Yang, *Nat. Electron.* **2018**, *1*, 137.
[232] K. M. Kim, D. S. Jeong, C. S. Hwang, *Nanotechnology* **2011**, *22*, 254002.
[233] K. Wiesenfeld, F. Moss, *Nature* **1995**, *373*, 33.
[234] B. J. Gluckman, T. I. Netoff, E. J. Neel, W. L. Spano, M. L. Spano, S. J. Schiff, *Phys. Rev. Lett.* **1996**, *77*, 4098.
[235] D. Nozaki, D. J. Mar, P. Grigg, J. J. Collins, *Phys. Rev. Lett.* **1999**, *82*, 2402.
[236] X. J. Wang, *Physiol. Rev.* **2010**, *90*, 1195.
[237] G. Deco, E. T. Rolls, R. Romo, *Prog. Neurobiol.* **2009**, *88*, 1.
[238] F. Cai, J. M. Correll, S. H. Lee, Y. Lim, V. Bothra, Z. Zhang, M. P. Flynn, W. D. Lu, *Nat. Electron.* **2019**, *2*, 290.
[239] F. Cai, S. Kumar, T. Van Vaerenbergh, X. Sheng, R. Liu, C. Li, Z. Liu, M. Foltin, S. Yu, Q. Xia, J. J. Yang, R. Beausoleil, W. D. Lu, J. P. Strachan, *Nat. Electron.* **2020**, *3*, 409.
[240] T. Hasegawa, K. Terabe, T. Tsuruoka, M. Aono, *Adv. Mater.* **2012**, *24*, 252.
[241] H. Hihara, A. Iwasaki, M. Hashimoto, H. Ochi, Y. Mitsuyama, H. Onodera, H. Kanbara, K. Wakabayashi, T. Sugibayashi, T. Takenaka, H. Hada, M. Tada, M. Miyamura, T. Sakamoto, in *Atomic Switch* (Ed: M. Aono), Springer, Cham, Switzerland **2020**, p. 33.
[242] A. Emboras, J. Niegemann, P. Ma, C. Haffner, A. Pedersen, M. Luisier, C. Hafner, T. Schimmel, J. Leuthold, *Nano Lett.* **2016**, *16*, 709.
[243] A. Emboras, A. Alabastri, F. Ducry, B. Cheng, Y. Salamin, P. Ma, S. Andermatt, B. Baeuerle, A. Josten, C. Hafner, M. Luisier, P. Nordlander, J. Leuthold, *ACS Nano* **2018**, *12*, 6706.
[244] E. Göbel, U. Siegner, *The New International System of Units (SI)*, Wiley, New York **2019**.
[245] J. Fischer, J. Ullrich, *Nat. Phys.* **2016**, *12*, 4.
[246] a) SI logo, https://www.bipm.org/en/measurement-units/si-promotion (accessed: April 2022); b) G. Milano, F. Ferrarese Lupi, M. Fretto, C. Ricciardi, N. De Leo, L. Boarino, *Adv. Quantum Technol.* **2020**, *3*, 2000009.
[247] BIPM Bureau International des Poids et Mesures, The International System of Units (SI Brochure), 9th ed., **2019**, https://www.bipm.org/documents/20126/41483022/SI-Brochure-9-EN.pdf (accessed: April 2022).
[248] L. X. Zhang, J. P. Leburton, R. Hanson, L. P. Kouwenhoven, *Appl. Phys. Lett.* **2004**, *85*, 2628.

Gianluca Milano is currently a permanent researcher at the Italian National Institute of Metrological Research (INRiM). He received a Ph.D. in physics cum laude from Politecnico di Torino, Italy, in collaboration with the Italian Institute of Technology (IIT). His main research interests and activities focus on: i) the investigation of electronic and ionic transport properties and physicochemical phenomena in nanodevices and low dimensional systems; and ii) memristive devices and architectures for memory and neuromorphic applications, from material synthesis to device characterization, modeling, and implementation of unconventional and brain-inspired computing paradigms.

Ilia Valov is currently head of group Nanoelectrochemistry at the Research Centre Jülich. He received Dr. rer.nat. degree at Justus-Liebig-University in Gießen, Germany. His research interests and activities are concentrated on electrochemical and, in general, physicochemical phenomena at the nano- and sub-nanoscale, such as mass and charge transport, electric double layer, point defects, surfaces, and interfaces with a focus on resistive switching memories, memristive and neuromorphic devices, and energy conversion and electrocatalysis (water splitting). A special focus in the research is set on the relation between materials chemistry, structure and properties, materials design, and particular applications and functionalities.